Editors' Suggestion

Lattice Hamiltonians and stray interactions within quantum processors

Xuexin Xu,[1,*] Manabputra,[2] Chloé Vignes,[1,3] Mohammad H. Ansari,[1] and John M. Martinis[4,5]

[1] *Peter Grünberg Institute, PGI-2, Forschungszentrum Jülich, 52428 Jülich, Germany*

[2] *Department of Physics, Syracuse University, Syracuse, New York 13244, USA*

[3] *Department of Electrical Engineering and Computer Science, Massachusetts Institute of Technology, Cambridge, Massachusetts 02139, USA*

[4] *Department of Physics, University of California, Santa Barbara, Santa Barbara, California 93106, USA*

[5] *Qolab, Inc, 9854 National Blvd, 1436, Los Angeles, CA 90034, USA*

(Received 5 April 2024; revised 31 October 2024; accepted 4 November 2024; published 10 December 2024)

Developing Hamiltonian models for quantum processors with many qubits on the same chip is crucial for advancing quantum computing technologies. Stray couplings between qubits lead to errors in gate operations. This study underscores the importance of incorporating lattice Hamiltonians into quantum circuit design. By comparing many-body effects with two-body stray couplings, we show how adjusting circuit parameters can increase two-qubit-gate fidelity. We find that loosely decoupled qubits result in weaker stray interactions and higher gate fidelity, challenging conventional assumptions. We investigate the scenario where three-body *ZZZ* interaction surpasses two-body *ZZ* interactions, highlighting the transformative potential of lattice Hamiltonians for novel multiqubit gates. Moreover, we investigate the cross-resonance gate within the lattice-Hamiltonian framework and examine the impact of microwave pulses on stray coupling. This emphasizes the necessity of developing a comprehensive theoretical framework that includes lattice interactions, which are now critical given the sophistication of contemporary quantum hardware. These insights are vital for developing fault-tolerant quantum computing and next-generation quantum processors.

DOI: 10.1103/PhysRevApplied.22.064030

I. INTRODUCTION

A significant number of qubits and their precise control are essential for practical quantum computations to be feasible. A major challenge in increasing the number of qubits in a quantum processor involves reducing the interference caused by stray couplings from neighboring qubits. This noise interferes with gate operations, often resulting in errors surpassing the acceptable error-correction thresholds [1–3]. These inaccuracies primarily stem from the difficulties in achieving both rapid and accurate gates, exacerbated by unwanted interactions between qubits [4–6].

One-qubit and two-qubit gates are foundational for universal quantum computation, and several strategies have been developed to improve their performance [7–10]. However, they are not the only gates available [11]. Multiqubit interactions, such as Toffoli gates, together with other gates, can make a different universal set [12]. Although multiqubit gates do not scale well and may incur additional overhead when one is constructing many target algorithms, their primary benefit lies in the ability to entangle more than two qubits simultaneously. This capability, in contrast to the use of a sequence of one-qubit and two-qubit gates, can accelerate computation, reduce circuit depth, and ensure compatibility with state-of-the-art hardware, such as the implementation of multiqubit interactions using programmable algorithms or in a qudit system. [13–21]. If low-error multiqubit gates can be made and executed, several areas of research will be positively impacted, such as quantum chemistry [22] and machine learning [23,24]. Beyond the interesting prospect of taming multiqubit interactions as novel gates, one can acknowledge that such interactions can have detrimental effect on two-qubit gates. The effect of multiqubit interactions on two-qubit-gate performance, whether subtle or significant, is yet to be fully determined.

In the context of quantum computing, the performance of two-qubit gates is primarily modeled by circuit-quantum-electrodynamics (cQED) theory, which tends to overlook the effects of multiqubit interactions, suggesting that their influence is pronounced only at higher orders [25]. Several studies have explored the role of multiqubit interactions in quantum systems [26–28]. Many-body systems exhibit a propensity for long-range correlations, indicating that qubit connectivity enhances delocalization. Recent findings demonstrate the potential for chaos in many-qubit processors within certain parameters, prompting consideration of many-body-localization (MBL) theory as a crucial tool [29–31]. However, this

*Contact author: x.xu@fz-juelich.de

approach underestimates the true strength of multiqubit interactions, highlighting the need for more-sophisticated theoretical frameworks. Understanding and effectively managing these interactions is crucial for the advancement of quantum processors [32,33].

In this study, we demonstrate that the presumed hierarchy of many-body interactions is not valid, even within the parameters of quantum computation. Our findings indicate that multiqubit interactions can be as significant as two-qubit interactions. Further exploration of multiqubit interactions is essential to understand the adverse effects of three-body entanglement on pairwise interactions. This paper is organized as follows: First, we study multiqubit interactions in a qubit lattice, particularly emphasizing the importance of considering the three-body *ZZZ* interaction. In Sec. III, we validate our model by evaluating *ZZZ* in an actual experimental setup in a three-qubit lattice. In Sec. IV, we generalize our nonperturbative approach in a triangular lattice of three qubits with three couplers, and highlight scenarios in circuit parameters where attempts to reduce two-qubit-gate errors may unintentionally amplify three-body interactions, thereby posing a challenge in increasing gate fidelity. In Sec. V, we identify specific conditions under which three-body interactions prevail over two-body interactions. Finally, we study cases of microwave-driven gates in practical devices and show they can largely benefit from one tuning circuit parameters by reducing nonlocal parasitic interactions.

II. LATTICE HAMILTONIAN

In quantum processors, qubits are positioned at the vertices of an underlying spatial lattice and interact by intentional couplings along the lattice's edges. Typically, the time variable is treated as continuous. The Hamiltonian of the processor acts as the generator of time evolution of the quantum state of the lattice, which is usually derived from the cQED formulation, involving a transformation of the processor's circuit Lagrangian.

A logical qubit comprises multiple physical qubits, typically arranged at the vertices of a lattice and interacting with their nearest neighbors [34–36]. This arrangement is predicated on the assumption that more-distant qubits interact weakly. However, in practice, distant qubits may exhibit significant interactions. For instance, in superconducting processors, distant qubits may interact via direct capacitance or inductance. Moreover, weakly interacting distant qubits with nearly matching frequencies can significantly influence each other, where activation of one qubit may lead to the excitation of another.

Modeling in cQED has traditionally centered on pairwise qubit interactions, often overlooking interactions between distant qubits in the effective circuit Hamiltonians.

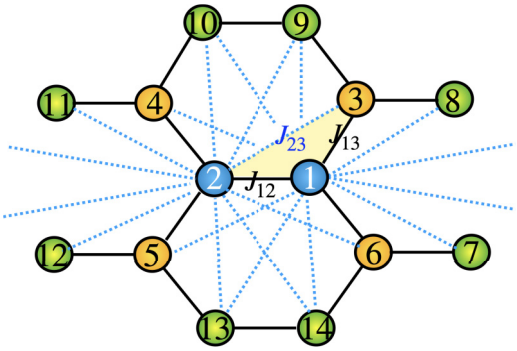

FIG. 1. In a standard hexagonal lattice design, qubits are situated at the vertices, and couplers are placed at the midpoint of each solid-line edge that connects the qubits. Dashed lines in this figure represent some unintentional couplings here; however, in principle, they exist everywhere in between every pair of qubits, making the lattice effectively an all-to-all lattice. The triangle highlighted in yellow exemplifies intentional couplings between qubits 1 and 2, as well as between qubits 1 and 3. However, this triangle is closed by incorporation of the unintentional interaction between qubits 2 and 3.

In 2D lattices, the fundamental building block can be a triangle, geometrically a two-simplex. For 3D lattices, the basic unit is a tetrahedron, or a three-simplex, and so forth. A 1D chain, for example, can be partitioned into line segments, which are one-simplices. Thus, in cQED, pairwise interactions on one-simplices are considered. Further extension of this concept allows the inclusion of interactions within two-simplices, encompassing every three qubits in the lattice.

Figure 1 illustrates a typical hexagonal lattice with qubits at the vertices, interacting along the edges with their nearest neighbors. Such configurations are instrumental in developing quantum error-correcting codes, such as the triangular color code [37]. Compared with traditional codes, this model boasts benefits in scalability and error threshold [38,39].

Modeling a quantum processor begins with formulating Hamiltonian terms for every lumped electronic element in the lattice and understanding the nature of their interactions. This Hamiltonian is then subjected to various transformations and simplifications, ultimately being distilled into an effective Hamiltonian. In this reduced form, the couplers are typically omitted, and the focus is on the two-level qubits and their effective coupling strengths. This process establishes the computational lattice Hamiltonian. The more-comprehensive examination of the detailed circuit, which includes both qubits and couplers, is reserved for the next section, in which we study the example of a triangular lattice made with three qubits and three couplers located between every pair of qubits.

We investigate a qubit lattice as shown in Fig. 1, characterized by its hexagonal patterns. The qubits are color-coded for clarity. Analyzing hexagonal geometries poses significant challenges due to their inherent complexity. To facilitate a comprehensive understanding, we initially focus on the simplest form of multiqubit interaction: the three-qubit interaction. Our primary attention is on the blue qubits, labeled 1 and 2, surrounded by orange qubits numbered 3–6. These orange qubits exhibit *intentional* coupling strengths with qubits 1 and 2, as indicated by solid lines. This lattice is deliberately designed and fabricated to establish intentional couplings between qubits.

However, it is reasonable to consider that there is a level of weak coupling between every pair of qubits, possibly due to factors such as weak capacitive interactions. The presence of such unintentional couplings between all pairs of qubits is significant. In Fig. 1, these *unintentional* interactions are marked by dashed lines. The green qubits, labeled 7–14, while not having intentional couplings with qubits 1 and 2, are nonetheless interconnected through unintentional couplings. For instance, in the triangle highlighted in yellow, the coupling strengths J_{12} and J_{13} are intentional, whereas J_{23} represents an unintentional but nonzero coupling. Theoretically estimating these coupling strengths necessitates a detailed understanding of the lattice's complete structure, including all couplers, which is discussed in the next section.

The lattice, encompassing both intentional and unintentional interactions, forms a nearly-all-to-all interaction network. A straightforward method to derive the lattice Hamiltonian starts with the Hamiltonian of electronic lumped elements in the full Hilbert space, typically limited to two-body interactions. The extensive Hilbert-space Hamiltonian is described as [40,41]

$$\frac{H}{\hbar} = \sum_{q,n_q} \tilde{\omega}_q(n_q)|n_q\rangle\langle n_q| + \sum_{p,q,m_p,n_q} \sqrt{(m_p+1)(n_q+1)} \times J_{pq}^{m_p n_q}(|m_p, n_q+1\rangle\langle m_p+1, n_q| + \text{H.c.}), \quad (1)$$

where p and q are indices labeling qubits, while m_p and n_q denote their respective energy levels. The frequency $\tilde{\omega}_q(n_q)$ represents the effective energy difference between levels n_q and n_q+1, i.e., $\hbar\tilde{\omega}_q(n_q) = E(n_q+1) - E(n_q)$. The tilde differentiates effective qubit frequencies in the reduced circuit. The qubits exhibit a nonharmonic energy spectrum, leading to anharmonicity defined as $\tilde{\delta}_q = \tilde{\omega}_q(1) - \tilde{\omega}_q(0)$.

The coupling strength, denoted as $J_p^{m_p,n_q}$, represents the net coupling strength between qubits p and q. This strength is influenced by both the energy difference between the qubits and the individual energy levels of each qubit. It comprises *direct* and *indirect* components, with the latter representing the coupling mediated by a coupler element, such as a transmission line, cavity, or another qubit. On the lattice, as described above, the solid edges represent intentional couplings and include the sum of both direct and indirect couplings. In contrast, the dashed lines, which indicate unintentional couplings, consist only of direct coupling.

The extensive Hilbert-space Hamiltonian of Eq. (1) can be projected onto the computational Hamiltonian (Details can be found in Appendix B.). This projection usually maps the level repulsion/attraction between computational and noncomputational levels into interactions involving more than two qubits in the Pauli basis. In a lattice consisting of a total of N qubits, a block-diagonalization transformation is used to perform this projection [42,43]. The final Hamiltonian in the computational basis can be formally represented by the following effective Hamiltonian:

$$\frac{H_{\text{eff}}}{\hbar} = \sum_{\substack{\text{qubit}\\ i}} \tilde{\omega}_i \frac{\hat{Z}_i}{2} + \sum_{\substack{\text{two qubits}\\ i,j}} \alpha_{ij} \frac{\hat{Z}_i\hat{Z}_j}{4} + \sum_{\substack{\text{three qubits}\\ i,j,k}} \alpha_{ijk} \frac{\hat{Z}_i\hat{Z}_j\hat{Z}_k}{8}. \quad (2)$$

In Eq. (2), we limit our analysis to three-body entangling interactions. The numerous noncomputational energy levels present in the original Hamiltonian (1) manifest themselves in the effective Hamiltonian, Eq. (2), as stray couplings, such as ZZ and ZZZ. These couplings do not cause state transitions in qubits, but they can accumulate phase errors in quantum states across different levels of entanglement. As these interactions are constantly active, their collective effect on the phase is continuous and pervasive.

In our study, we analyze the stray-coupling ZZ interaction between qubits i and j by separating the contributions of two-body and three-body interactions. The two-body contribution, denoted as ζ_{ij}, is relatively straightforward to compute [6,44–46]. The quantity ζ_{ijk} is the three-body stray-entanglement coupling, and quantifies the stray entanglement that can distort the intentional entanglement between three qubits. To evaluate the influence of three-body interactions on the ZZ-interaction strength, it is essential to consider all potential third qubits, whether they interact intentionally or unintentionally with qubits i and j. As depicted in Fig. 1, we operate under the assumption that all qubits are interconnected. This leads us to infer that qubits i and j are part of triangular interactions with numerous third qubits, labeled as k for clarity. Hence, the overall ZZ interaction in a network of multiple qubits is calculated as

$$\alpha_{ij} = \zeta_{ij} + \sum_k \zeta_{ijk}. \quad (3)$$

The strength of the three-body operation ζ_{ijk} will correspond to the operator $\hat{Z}_i\hat{Z}_j\hat{I}_k$ within the triangle formed by

interacting qubits i, j, and k, which makes it eligible to be added to ZZ interaction as a three-body contribution.

However, the ZZ term is not the only stray coupling one can consider for a circuit of qubits. In the Hamiltonian (2), we generalized our analysis beyond the traditional focus of pairwise stray couplings to also include three-body stray entangling interactions, denoted as ZZZ. Essentially, in a lattice comprising N qubits, the effective Hamiltonian can encompass all stray entangling interactions, up to N-body interaction. Nonetheless, for practical simplicity, we examine the effects up to three-body interactions within a lattice of multiple qubits.

1. Two-body ZZ interaction

In this section, we assess the parasitic interactions between the two blue qubits depicted in Fig. 1. Initially, we use a perturbative approach to estimate the coupling strength.

Within the perturbative regime of coupling strengths $|J_{pq}/[\omega_p - \omega_q]| \ll 1$, namely, the "dispersive regime," one can show the following two useful symmetries:

$$\begin{aligned} &J_{ij}^{mn} = J_{ji}^{nm} \quad \text{for all } n, m \in \{0, 1, 2, \ldots\}, \\ &J_{ij}^{01} + J_{ij}^{10} = J_{ij}^{00} + J_{ij}^{11}. \end{aligned} \tag{4}$$

In the following section, we introduce another relationship between different J values, as detailed in Eq. (11), after discussing the coupler specifics. In Appendix C, we numerically validate the identities by simulating both sides of the equations and verifying their equalities.

By using perturbation theory, one can calculate the two-body ZZ coupling strengths up to the third order in J as follows:

$$\zeta_{ij}/2 \equiv \frac{(J_{ij}^{01})^2}{\Delta_{ij}^{01}} - \frac{(J_{ij}^{10})^2}{\Delta_{ij}^{10}}, \tag{5}$$

$$\begin{aligned} \zeta_{ijk}/4 \equiv &\frac{J_{ij}^{00} J_{ik}^{00} J_{jk}^{00}}{\Delta_{ik}^{00} \Delta_{jk}^{00}} + \frac{J_{ij}^{00} J_{ik}^{01} J_{jk}^{01}}{\Delta_{ik}^{01} \Delta_{jk}^{01}} \\ &- \frac{J_{ij}^{01} J_{ik}^{00} J_{jk}^{10}}{\Delta_{ik}^{00} \Delta_{jk}^{10}} - \frac{J_{ij}^{10} J_{ik}^{10} J_{jk}^{00}}{\Delta_{ik}^{10} \Delta_{jk}^{00}} - K(1), \end{aligned} \tag{6}$$

with $\Delta_{ij}^{m_i n_j} = \tilde{\omega}_i(m_i) - \tilde{\omega}_j(n_j)$, defined as the energy difference between the transitions $|m_i + 1\rangle \leftrightarrow |m_i\rangle$ of qubit i and $|n_j + 1\rangle \leftrightarrow |n_j\rangle$ of qubit j.

Using Eq. (4) and $\Delta_{ij}^{m_i n_j} = -\Delta_{ji}^{n_j m_i}$, one can show that ζ_{ij} and ζ_{ijk} are both symmetric under switching $i \leftrightarrow j$, (i.e., $\zeta_{ij} = \zeta_{ji}$ and $\zeta_{ijk} = \zeta_{jik}$), indicating that ZZ interaction between qubits i and j is symmetric with respect to interchanging the qubit labels $i \leftrightarrow j$.

In Eq. (6), $K(n)$ is a scalar number, and is defined as follows:

$$K(n) = -\sum_{\substack{i,j,k=\{1,2,3\} \\ (i<j;\ i,j\neq k)}} \frac{J_{ij}^{nn} J_{ik}^{n,1-n} J_{jk}^{n,1-n}}{\Delta_{ik}^{n,1-n} \Delta_{jk}^{n,1-n}},$$

which depends in the leading order on J^3/Δ^2.

For example, in a chain of qubits, without one considering unintentional couplings, the three-body and higher couplings are identically zero, which is due to the absence of symplectic interaction. One can see in Eq. (6) that even a small triangularity makes ζ_{ijk} nonzero, which can even be significant for nearly-in-resonance qubits.

2. Three-body ZZZ interaction

In a circuit with at least three qubits in triangular interactions, perturbation theory estimates the following ZZZ-interaction strength, which is a one-shot three-body interaction:

$$\alpha_{ZZZ}/8 = \sum_{n=0,1} K(n). \tag{7}$$

The perturbative three-body ZZZ interaction is generally considered to be weaker than two-body ZZ interactions. This is attributed to the higher-order dependence of the three-body interaction compared with the two-body interaction within the perturbative parameter $J/\Delta < 1$. Such an observation is consistent with MBL theory, as highlighted in various key studies. MBL theory suggests a distinct hierarchy of interaction scales in weakly interacting spins. In a triangular configuration of superconducting qubits, the nearest-neighbor ZZ interactions are typically the most pronounced, with the ZZZ couplings being considerably weaker.

However, beyond the dispersive regime, qubit-qubit interactions are stronger, as detailed in Ref. [43]. For instance, when the frequency of the coupler approaches that of the qubits, the strength of both two-body and three-body interactions may challenge the established MBL hierarchy. Specifically, this could lead to a scenario where α_{ZZZ} is equal to or greater than α_{ZZ}, a phenomenon we refer to as "ZZZ superiority." Interestingly, this superiority might even occur within the dispersive regime, as shown in Fig. 2.

To illustrate this, we consider a triangular circuit comprising three qubits, each with a uniform pairwise coupling strength J and anharmonicity δ. By comparing the strength of the ZZZ interaction as described in Eq. (7) with the strength of the ZZ interaction as per Eq. (3), we can identify the conditions under which ZZZ superiority emerges. Figure 2 displays these conditions for various frequency settings of Δ_{31}: $-\Delta_{32}$, $0.5\Delta_{32}$, $1.2\Delta_{32}$, and $3\Delta_{32}$. These

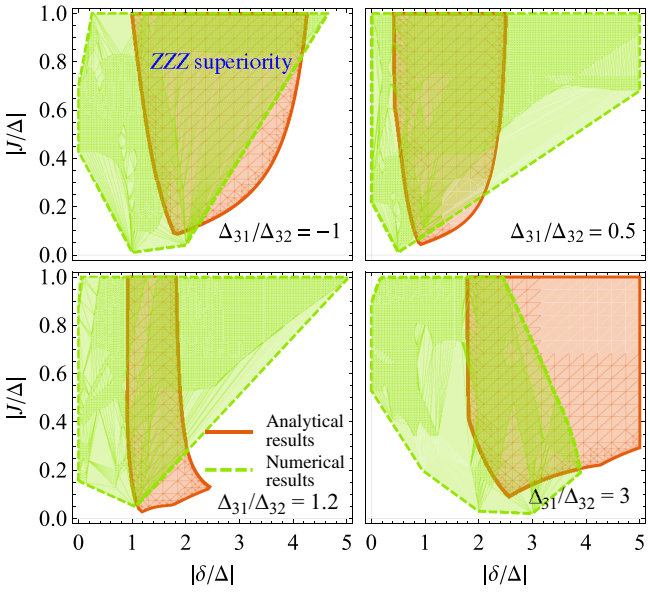

FIG. 2. Phase diagram of ZZZ superiority where $|ZZZ| > |ZZ|_{\max}$ as a function of coupling strength $|J/\Delta|$ and anharmonicity $|\delta/\Delta|$ at different qubit frequency detunings with $\Delta = \Delta_{32}$. The shaded area represents the region (red for perturbative SWT and green for nonperturbative numerical analysis) where three-body ZZZ interaction is superior to two-body ZZ interaction.

scenarios are represented analytically in red regions with use of the Schrieffer-Wolff transformation (SWT) and are compared with green regions, which depict numerical analysis results obtained by our diagonalizing the Hamiltonian (1). The discrepancy arises from the breakdown of the perturbative SWT beyond the dispersive regime.

III. A THREE-QUBIT LATTICE

Considering that an all-to-all lattice of qubits can be divided into numerous triangular building blocks, we specifically focus on one such triangle in this section. In this triangle, three qubits are pairwise connected through three couplers. Moreover, we also account for direct couplings between the qubits, as depicted in Fig. 3. The effective Hamiltonian is calculated by both the perturbative approach and the nonperturbative approach. A systematic comparison is then made between scenarios with and without the inclusion of a third qubit. This comparative analysis is instrumental in understanding the nuances of qubit interactions within such a lattice configuration.

Under the parameters typically used in quantum computing, we interestingly uncover the alteration of multiqubit-interaction-strength hierarchy. This provides key insights into the complex dynamics of qubit interactions and challenges prevailing assumptions about how these interactions are organized and prioritized within quantum systems.

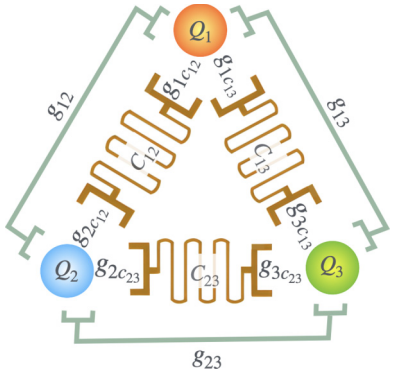

FIG. 3. A typical triangle of three qubits $Q1, Q2$, and $Q3$, which pairwise interact in a combination of direct couplings g_{ij} and indirect couplings g_{ic_r} via the couplers C_r.

In Fig. 3, qubits are represented by circles and are labeled as Q_q, $q = \{1, 2, 3\}$. The rectangles symbolize the couplers C_r, with $r = \{12, 23, 13\}$ indicating the labels of the two qubits they mutually couple to intentionally. The coupling strength between a qubit Q_q and a coupler C_r is denoted as g_{qc_r}. Qubits interact indirectly through their shared coupler, yet they can also have direct interactions, such as capacitive ones. The direct coupling between qubit q and another qubit q' is represented as $g_{qq'}$.

For simplicity in our analysis, we assume all couplers function like harmonic oscillators, akin to transmission lines or cavity modes. In the model for Fig. 3, we ignore the weak interactions between qubits and distant resonators. This means we consider $g_{1c_{23}} = g_{2c_{13}} = g_{3c_{12}}$ as negligible or equal to zero. Thus, we express the circuit Hamiltonian in our study as follows:

$$\frac{H}{\hbar} = \sum_q \omega_q \hat{a}_q^\dagger \hat{a}_q + \frac{\delta_q}{2} \hat{a}_q^\dagger \hat{a}_q (\hat{a}_q^\dagger \hat{a}_q - 1) + \sum_r \omega_{c_r} \hat{c}_r^\dagger \hat{c}_r + \sum_{r,q,q'} \left[g_{qq'} (\hat{a}_q - \hat{a}_q^\dagger) + g_{qc_r} (\hat{c}_r - \hat{c}_r^\dagger) \right] (\hat{a}_{q'} - \hat{a}_{q'}^\dagger), \tag{8}$$

with ω_q being the bare qubit frequency, δ_q the qubit anharmonicity, and ω_{c_r} the coupler frequency. To obtain the analytical Hamiltonian between qubits in the computational subset, first we restrict circuit parameters within the dispersive regime, i.e., $g_{qc_r} \ll |\omega_{c_r} - \omega_q|$, and use the Schrieffer-Wolff block diagonalization, which helps to make the Hilbert space of harmonic couplers separable from the qubit subset; therefore, couplers can be safely eliminated, and their effect renormalizes the bare qubit frequency into the dressed values:

$$\tilde{\omega}(n_q) = \left(\omega_q + \frac{(n_q - 1)\delta_q}{2} \right) n_q - \sum_r \frac{g_{qc_r}^2 n_q}{\Delta_{c_r q}(n_q - 1)}, \tag{9}$$

with r summing over those resonators that interact with qubit q via g_{qc_r}. We define $\Delta_{c_r i}(m_i) \equiv \omega_{c_r} - \omega_i - m_i\delta_i$.

Two qubits q and q' that share the same coupler C_r and couple to it by the strengths g_{qc_r} and $g_{q'c_r}$ effectively interact with one another with the following effective strength:

$$J_{qq'}^{m_q n_{q'}} = g_{qq'} - \frac{g_{qc_r} g_{q'c_r}}{2}\left(\frac{1}{\Delta_{c_r q}(m_q)} + \frac{1}{\Delta_{c_r q'}(n_{q'})}\right), \tag{10}$$

with $g_{qq'}$ being the direct (i.e., capacitive) coupling strength between the two qubits and the second term being the perturbative indirect-coupling strength via the shared coupler.

A few lines of algebra prove the validity of the two identities in Eq. (4), and a third one below, which turn out to be a useful set of relations for simplifying problems:

$$J_{ij}^{01} - \beta_{ij} J_{ij}^{10} = \left(1 - \beta_{ij}\right) J_{ij}^{00}, \tag{11}$$

with $\beta_{ij} = (\delta_j/\delta_i)\Delta_{ci}(0)/\Delta_{cj}(0)(\Delta_{ci}(1)/\Delta_{cj}(1))$ and $\beta_{ji} = 1/\beta_{ij}$.

We can assess both two-body and three-body interactions within the simplified three-qubit circuit, using parameters determined in the dispersive regime. Figures 4(a)–4(c) illustrate the dependency of the ZZ interaction on the frequency (whether bare or dressed) of a specific qubit, in this case, Q_2. Figure 4(d) presents the results for the three-body ZZZ interaction as per Eq. (7). The precision of our theoretical derivation is corroborated by the results of our numerical simulations.

Figures 4(a)–4(c) display the theoretical estimation of two-qubit ZZ interactions among different pairs in a triangular qubit configuration, with the variation of frequency in qubit Q_2. The dashed green lines represent second-order perturbative results, which take into account only pairwise interactions only up to J^2 [47]. The solid blue lines show perturbative results based on Eqs. (5) and (6) up to third order in J, in which naturally three-qubit correction terms $K(n)$ are included. Furthermore, red asterisks indicate our numerical nonperturbative results, obtained with the use of CirQubit. This comprehensive approach provides a deeper understanding of the interaction dynamics within the qubit triangle.

Comparison of the two perturbative analyses—one focusing solely on pairwise interactions and the other encompassing three-body interactions—provides valuable insights into the influence of multiqubit interactions on quantum device performance. In scenarios where the frequency ω_2 is considerably distinct from the frequencies of the other two qubits, the analytical and numerical results align closely. This suggests that the impact of three-body corrections is relatively minor in such a domain of frequencies.

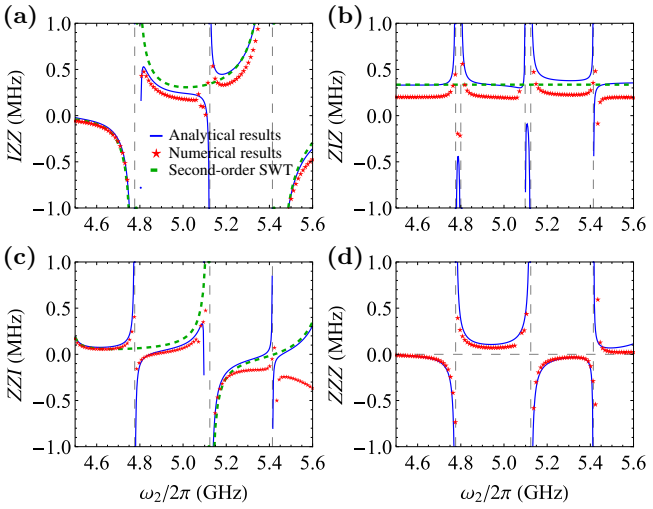

FIG. 4. Two-body ZZ interaction and three-body ZZZ interaction in a three-qubit circuit with all-to-all connectivity. Solid lines represent the analytical results for ZZ interaction in Eq. (3) and ZZZ interaction in Eq. (7), while the dashed lines correspond to the second-order SWT results in Eq. (5) for ZZ interaction, with no contribution to ZZZ interaction since first-order and second-order terms are both zero, while asterisks show numerical simulation results by diagonalization of Eq. (8). Circuit parameters are as follows: $\omega_1/2\pi = 4.8$ GHz, $\omega_3/2\pi = 5.1$ GHz, $\delta_1/2\pi = \delta_2/2\pi = \delta_3/2\pi = -330$ MHz, $\omega_{c_{12}}/2\pi = 5.8$ GHz, $\omega_{c_{23}}/2\pi = 6.1$ GHz, $\omega_{c_{13}}/2\pi = 5.7$ GHz, $g_{1c_{12}}/2\pi = g_{1c_{13}}/2\pi = g_{2c_{12}}/2\pi = g_{3c_{13}}/2\pi = 85$ MHz, $g_{2c_{23}}/2\pi = g_{3c_{23}}/2\pi = 102$ MHz, and direct qubit-qubit coupling $g_{12}/2\pi = g_{23}/2\pi = 4$ MHz and $g_{13}/2\pi = 6$ MHz.

However, as the frequency of Q_2 approaches that of another qubit, the results based solely on pairwise interactions deviate from the other two results, the three-body formulation and numerical data. Interestingly, Eqs. (5) and (6), which incorporate three-body interactions, continue to provide a reasonable approximation to the numerical interaction strength, even near points of discontinuity. The numerical Hamiltonian evaluates finite points in proximity to divergences, typically where quantum states are nearly degenerate.

Interestingly, as shown in Figs. 4(a) and 4(c), the interactions IZZ and ZZI can be nullified at two distinct Q_2 frequencies. These specific frequencies are accurately predicted by Eqs. (5) and (6), underscoring the effectiveness of these equations in capturing the nuances of multiqubit interactions in quantum systems.

In Fig. 4(b), the ZIZ interaction predominantly maintains a positive value across a wide range of Q_2 frequencies, with the exception of a few specific frequencies where the system is nearly degenerate. It is important to note that the primary contribution to the ZIZ interaction originates from Q_1 and Q_3, rather than Q_2. The gap of approximately 100 kHz between the analytical formula and the numerical

simulation results, persists even in a well-defined dispersive regime where Q_2's frequency is distinctly separate from the frequencies of the other qubits. This discrepancy can be attributed to the omission of higher-order corrections in the Schrieffer-Wolff transformation. This transformation is used perturbatively to decouple resonators. More details can be found in Appendix D. By our including higher-order decoupling of resonators, the results become more consistent with the numerical simulations, thereby increasing the accuracy of the analytical approach.

Our nonperturbative analysis, illustrated by the red asterisks in Fig. 4(d), supports the conventional hierarchy where the strength of *ZZZ* interactions is weaker than that of *ZZ* interactions in circuits with specific frequency arrangements, such as $\omega_2 < \omega_1 < \omega_3$ or $\omega_1 < \omega_3 < \omega_2$. However, under certain frequency configurations, notably $\omega_1 < \omega_2 < \omega_3$, the strength of *ZZZ* interactions can exceed that of *ZZ* interactions such as *ZZI* interaction.

Our findings from examining lattice stray couplings challenge the widely held belief that higher-order interactions are always much weaker. This suggests that there might be an oversight in conventional quantum simulations. Traditionally, efforts have been focused primarily on minimizing *ZZ* interactions as a means to increase gate fidelity. However, our study indicates that this approach could be misleading. In certain circuit configurations, *ZZZ* interactions can play a significant role, potentially leading to unwanted entanglement. This realization underscores the need for a more-comprehensive consideration of various interaction types in the design and analysis of quantum systems, emphasizing that a broader perspective is essential for optimizing the performance and accuracy of quantum computing technologies.

Briefly, our study delves into the expanded scope of stray couplings beyond the *ZZ* interaction, focusing specifically on the three-body *ZZZ* interaction in an existing multiqubit device. This approach marks a departure from previous research, which predominantly concentrated on two-body interactions among three qubits and introduced nonsimultaneous three-qubit gates. Our investigation thus broadens the understanding of multiqubit interactions, particularly emphasizing the significance and characteristics of three-body interactions in quantum computing systems.

IV. *ZZ* GATE IN A TRIANGLE

In quantum circuits, the operation of a two-qubit gate, such as one involving qubits 2 and 3 in a triangular lattice as depicted in Fig. 3, can be significantly affected by the presence of additional qubits, such as qubit 1 in this scenario. The influence of such external qubits on gate performance typically arises through two main categories of interactions: (1) two-body interactions, which occur between qubits 1 and 2, or qubits 1 and 3, and (2) three-body interactions, involving all three qubits, qubits 2, 3, and 1, simultaneously.

Contrary to common belief, which regards three-body interactions as weaker than and often negligible compared with two-body interactions, this section emphasizes the need to consider three-body interactions in circuits. This consideration helps increase two-qubit-gate fidelity; furthermore, it may pave the way toward introducing meaningful instantaneous three-qubit gates. It is useful to categorize decoupling strategies into two distinct types: (1) Hard decoupling—this method aims to find an optimal operating point where the qubits involved in the gate operation are completely isolated, preventing even weak interactions with ungated qubits. The goal is to reach a state in which the coupling strength between the gated qubits and any additional, nonparticipating qubit is effectively null. (2) Soft decoupling—rather than striving for strict decoupling, we may focus on reducing stray couplings.

A critical aspect of our research involves conducting an extensive analysis of three-body lattice interactions among the qubits and assessing their impact on the performance of two-qubit gates. Each strategy has its own set of advantages and challenges. The choice between hard and soft decoupling often depends on the specific requirements of the quantum circuit and the nature of the qubits involved. We will understand in this section that the concept of hard decoupling might not always be feasible or even advantageous. Thus, our aim is to concentrate on mitigating the effects of these interactions instead of trying to eliminate them completely. This method is particularly useful in complex quantum circuits, where strict decoupling is challenging to achieve, or where selective interactions can contribute positively to the system's functionality.

A. Hard *J* decoupling

Consider the three-qubit system shown in Fig. 3. Each qubit in this system possesses multiple energy levels. Within the triangular lattice structure, a qubit Q_i can be excited from energy level n_i to energy level $n_i + 1$. This excitation can occur concurrently with the de-excitation of another qubit Q_j from energy level $m_j + 1$ down to energy level m_j. The strength of coupling $J_{ij}^{m_i,n_j}$ depends on a range of parameters related to both qubits and couplers.

The common belief is that the optimum operating point for a two-qubit gate within a triangular circuit is where two couplings are effectively turned off ("OFF"), while the third remains active ("ON"), thus establishing an "OFF-OFF-ON" state. To analyze the operating point of this two-qubit gate in the presence of a third interacting qubit, first we begin by setting J_{12}^{00} to zero, which is achievable at certain frequencies of the coupler C_{12}. This is what is namely "hard J decoupling," which is diagrammatically sketched in Fig. 5(a). In our simulation we apply the condition step

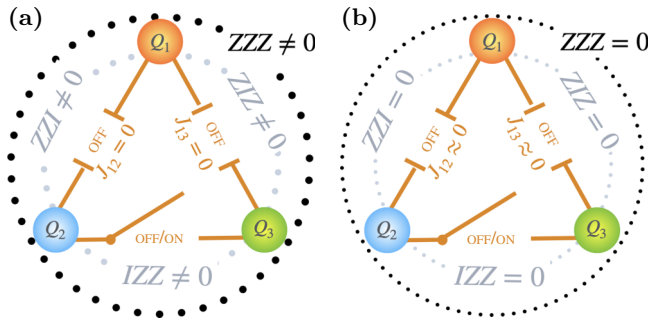

FIG. 5. (a) Hard J decoupling at $J_{12} = J_{13} \approx 0$ and (b) soft J decoupling at $J_{12} \approx 1$ MHz and $J_{13} = 0$.

by step: first we turn off coupling between Q_1 and Q_2, then between Q_1 and Q_3, and finally we switch on and off the controlled-Z gate between Q_2 and Q_3. Figure 6 showcases circuits with parameters outlined in the caption, all configured such that J_{12}^{00} is nullified. We then focus on turning off the second coupling, say, J_{13}^{00}, with its values indicated on the right axes of Fig. 6. Simultaneously, the third interaction, J_{23}^{00}, marked on the upper axes, is selected to be strong. The variation of these couplings is achieved by our adjusting the frequencies of the couplers C_{23} and C_{13}, as shown on the lower and left axes, respectively.

The color bars in Fig. 6 represent the strengths of two-body and three-body stray couplings. From left to right, the column corresponds to the following interactions: *ZZZ* (in green), *ZZI* (in blue), *ZIZ* (in red), and *IZZ* (in gray), which we evaluate nonperturbatively, [45,47–49]. Figure 6 is a valuable tool for identifying the optimal settings for achieving the desired gate operations, particularly where multiple interactions coexist and influence each other. This level of detailed analysis is crucial for the precise tuning of quantum circuits, enhancing their performance and increasing their reliability in various quantum computing applications.

We evaluate the interaction strengths of the *ZZ* and *ZZZ* couplings for the condition of $J_{12}^{00} = 0$, ensuring that Q_1 and Q_2 do not interact. In Fig. 6 we achieve the decoupling by testing two different values for direct capacitive coupling between Q_1 and Q_2, i.e., $g_{12}/2\pi = 4$ MHz and $g_{12}/2\pi = 13$ MHz in the upper and lower rows, respectively. Given the circuit parameters selected, the next coupling parameter to be neutralized is $J_{13}^{00} = 0$. The goal of this setting is to either preserve or enhance the coupling between Q_2 and Q_3, represented by J_{23}^{00}. This is achieved by our tuning the frequency of the coupler C_{13} within a range of 5.4–7 GHz. As a result, the coupling strength $J_{13}/2\pi$ varies from -3 to 9 MHz, reaching zero at the midpoint. Consequently, any point along the $J_{13} = 0$ line is characterized by a precise OFF-OFF interaction, which is critical for the intended gate operation.

Regarding the exclusive ON coupling, J_{23}^{00}, we modify the frequency of the coupler C_{23} by approximately 400 MHz on the lower axis. This adjustment leads to large $J_{23}^{00}/2\pi$ values that range from 15 to 30 MHz. We have marked three sample points with red circles and labeled them *A*–*C* in the upper row, corresponding to the weaker g_{12}, and *D*–*E* in the lower row, corresponding to the stronger g_{12}.

In exploring the stray *ZZ* and *ZZZ* couplings, we focus on the horizontal line corresponding to $J_{13} = 0$ in Fig. 6. This line signifies OFF-OFF interaction points achieved by our setting both J_{12}^{00} and J_{13}^{00} to zero. While this condition is intended to decouple Q_1 from Q_2 and Q_3, Fig. 6 illustrates that residual stray couplings still exist between Q_1 and the other two qubits, notably in *ZZZ* and *ZZI* configurations. This observation is crucial as it demonstrates that hard decoupling of seemingly noninteracting qubits does not necessarily lead to the elimination of stray couplings.

The persistence of these stray couplings is attributed to a significant factor. Although decoupling of two qubits, labeled i and j, is achieved by our setting their J_{ij}^{00} (computational-level coupling) to zero, these qubits remain indirectly coupled at their noncomputational levels. These levels include couplings such as J_{ij}^{01} and J_{ij}^{10}. It is these higher-order couplings that the stray interactions depend on. Thus, even when qubits are seemingly decoupled at their fundamental computational states, indirect couplings at other energy levels persist, leading to stray interactions that must be considered in quantum circuit design and operation. Details can be found in Appendix E.

The central aim of our study is to pinpoint "sweet spots" where both two-body and three-body stray couplings are minimal, specifically below 50 kHz. This quest is particularly evident in the last column in Fig. 6. Here, we highlight regions with low two-body *ZZ* interactions, where the maximum of $|ZZI|$ and $|ZIZ|$ remains under 50 kHz, as indicated by red-dashed boxes. Furthermore, areas showing both minimal *ZZZ* and residual *ZZ* couplings, characterized by the condition $\max\{|ZZI|, |ZIZ|, |ZZZ|\} <$ 50 kHz, are enclosed in green outlines.

The upper and lower plots in this column represent scenarios of weak and strong capacitive coupling between Q_1 and Q_2, denoted as g_{12}. In the case of weak g_{12}, all red-dashed boundaries converge, forming an extensive frequency range conducive to effectively decoupling Q_1 from the Q_2-Q_3 pair without significant stray couplings. This finding is particularly relevant for quantum devices designed for precise two-qubit-gate operations, such as the controlled-Z gate. Devices with such characteristics can smoothly transition from low to high *ZZ*-interaction values, while keeping spectator errors—errors affecting qubits not directly involved in the gate operation—to a minimum. This aspect is crucial for improving the overall performance and increasing the overall reliability of quantum gates in computational tasks.

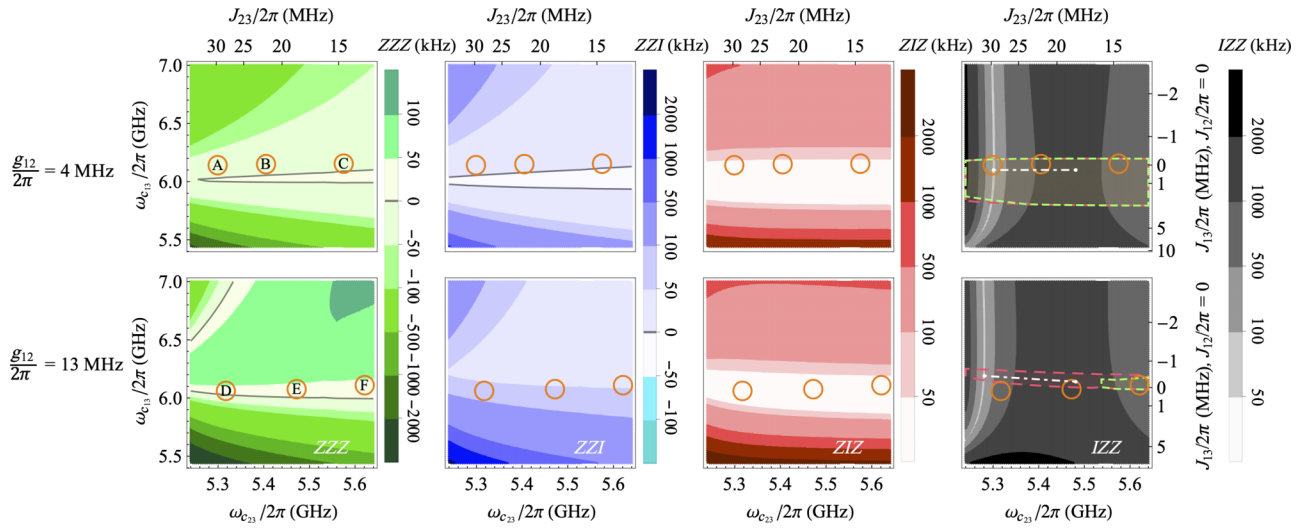

FIG. 6. Stray couplings in the triangular circuit with all-to-all connectivity calculated by our numerically diagonalizing the Hamiltonian (8) as a function of the frequencies of the resonators C_{23} and C_{13} i.e., $\omega_{c_{23}}$ and $\omega_{c_{13}}$, respectively. The first row is at $g_{12}/2\pi =$ 4 MHz with nearly zero J_{12} and J_{13} at point A with coupler frequencies $(\omega_{c_{12}}, \omega_{c_{23}}, \omega_{c_{13}})/2\pi = (6.66, 5.299, 6.141)$ GHz, point B with coupler frequencies $(\omega_{c_{12}}, \omega_{c_{23}}, \omega_{c_{13}})/2\pi = (6.67, 5.405, 6.15)$ GHz, and point C with coupler frequencies $(\omega_{c_{12}}, \omega_{c_{23}}, \omega_{c_{13}})/2\pi =$ $(6.68, 5.275, 6.154)$ GHz. The second row is at $g_{12}/2\pi = 13$ MHz with nearly zero J_{12} and J_{13} at point D with coupler frequencies $(\omega_{c_{12}}, \omega_{c_{23}}, \omega_{c_{13}})/2\pi = (5.438, 5.317, 6.021)$ GHz, point E with coupler frequencies $(\omega_{c_{12}}, \omega_{c_{23}}, \omega_{c_{13}})/2\pi = (5.443, 5.472, 6.076)$ GHz, and point F with coupler frequencies $(\omega_{c_{12}}, \omega_{c_{23}}, \omega_{c_{13}})/2\pi = (5.446, 5.621, 6.098)$ GHz. The shaded regions denote two intersections: $|ZZI| \cap |ZIZ| < 50$ kHz (light red) and $\max(|ZZI|, |ZIZ|, |ZZZ|) < 50$ kHz (light green), both on top of the IZZ interaction. Other circuit parameters are the same as in Fig. 4 with $\omega_2/2\pi = 5.0$ GHz.

In Fig. 6, the dotted-dashed white line within the red boundary, which represents a zone of low ZZ interaction, portrays an ideal trajectory for a parasitic-free ZZ gate operation between Q_2 and Q_3. This path transits from nearly zero on the left side to a strong value on the right side. Crucially, along this line, J_{12}^{00} and J_{13}^{00} are effectively zero, and both ZZI and ZIZ remain below 50 kHz, suggesting an efficient decoupling of Q_1 from the actively gated qubits, Q_2 and Q_3.

However, it is critical to take a careful look at the impact of ZZZ interactions for the gate. A comparison between the upper and lower plots in the last row in Fig. 6 reveals critical differences between weak and strong g_{12} regimes. In the weak g_{12} scenario (upper plot), the ideal gate trajectory is entirely within the green boundary, indicating that the three-body interaction is maintained below 50 kHz. This implies a safer operating zone where both two-body and three-body parasitic interactions are minimized. In contrast, in the strong direct coupling between Q_1 and Q_2 (lower plot), the gate path falls outside this low-ZZZ-interaction area. Here, the ZZZ value can potentially exceed 100 kHz, suggesting a heightened vulnerability to parasitic three-body interactions.

This observation reveals that one assuming that three-body ZZZ interactions are weaker than two-body ZZ interactions can lead to significant oversights in gate design. Suppression of parasitic two-body ZZ interactions may inadvertently introduce substantial errors from strong three-body interactions among presumed noninteracting qubits. Therefore, accurate assessment of three-body interactions is essential to avoid flawed designs and achieve high-fidelity quantum operations.

B. Soft J decoupling

The common desire in multiqubit circuit design is that during the application of a two-qubit gate, other qubits are silenced. This is usually interpreted as turning off J interaction between the gated qubits and other qubits. In the previous section, we examined this concept in the context of a triangular lattice by setting two pairwise interactions to zero and amplifying the third. In the previous section, we referred to this concept as "hard J decoupling." However, our detailed analysis reveals that the situation is significantly more complex than nullifying J interaction.

In this section, we explore the same OFF-OFF-ON interaction between Q_2 and Q_3 in an alternative setup: rather than enforcing a complete absence of interaction of these two qubits with Q_1, we allow some weak J interactions to occur if they contribute to reducing parasitic interactions. Our goal shifts towards minimizing stray-coupling strengths to the extent that they either disappear or become negligible (i.e., less than 50 kHz). Enforcing zero interaction between qubits is limited in scope; it only prevents interactions between two specific energy levels of one qubit with another qubit, which is inadequate to prohibit transitions across all energy levels. For instance, while

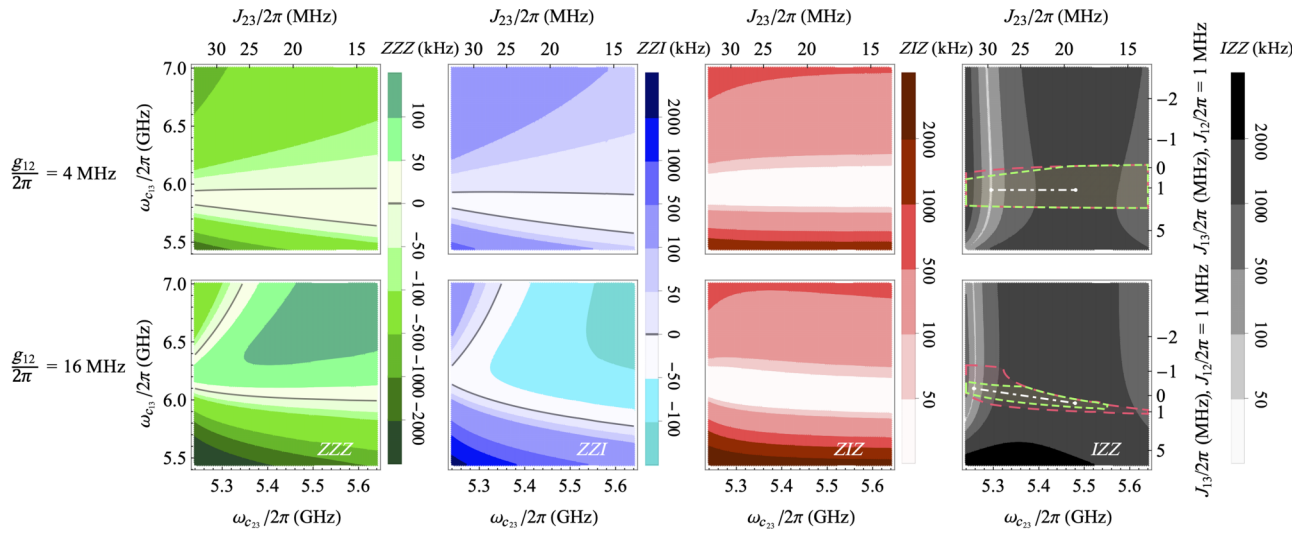

FIG. 7. Stray couplings in the triangular circuit with all-to-all connectivity calculated by our numerically diagonalizing the Hamiltonian (8) as a function of the frequencies of the resonators C_{23} and C_{13}, $\omega_{c_{23}}$ and $\omega_{c_{13}}$, respectively. The first row is at $g_{12}/2\pi =$ 4 MHz with weak $J_{12}/2\pi \approx 1$ MHz at $\omega_{c_{12}}/2\pi = 6.2$ GHz. The second row is at $g_{12}/2\pi = 16$ MHz with weak $J_{12}/2\pi \approx 1$ MHz at $\omega_{c_{12}}/2\pi = 5.3$ GHz. Other circuit parameters are the same as in Fig. 6.

hard decoupling might set J_{12}^{00} to zero, other coupling strengths, such as J_{12}^{01}, could still be nonzero. The so-called soft J decoupling is sketched diagrammatically in Fig. 5(b).

This realization implies that the idea of completely nullifying J interaction between qubits might be overly simplistic, if not altogether unachievable. Recognizing this limitation can shift the focus toward managing stray interactions rather than striving for complete noninteraction. In other words, we focus on the impact of relaxing one of the two OFF couplings to a near-OFF state, denoted as $\widetilde{\text{OFF}}$. This softer approach to qubit decoupling, or "soft J decoupling," is explored as a potentially-more-effective and potentially-more-realistic strategy for increasing ZZ interaction between Q_2 and Q_3, as opposed to the hard-decoupling strategy previously considered.

By setting the interaction between Q_1 and Q_2 to $J_{12}^{00}/2\pi = 1$ MHz, rather than completely zeroing it, we introduce a "soft-decoupling" criterion. Figure 7 illustrates how this can impact both two-body and three-body stray couplings in different circuit configurations: the first (second) row denotes a circuit with a weak (strong) direct capacitive coupling between Q_1 and Q_2, $g_{12} = 4$ MHz ($g_{12} = 16$ MHz). Such strength occurs at $\omega_{c_{12}}/2\pi = 6.2$ GHz ($\omega_{c_{12}}/2\pi = 5.3$ GHz).

The identification of "safe zones" for low stray couplings is crucial, which are identifiable in the last column in Fig. 7. These zones are defined by regions where all stray interactions are under 50 kHz. The region marked within the dashed green boundary in the final column presents zones exhibiting minimal stray couplings, both two body and three body. On comparison with scenarios of hard decoupling, it becomes evident that in the example of larger direct qubit-qubit coupling g_{12}, the zone of minimal stray interaction—termed the "stray safe zone"—extends over a broader area in conditions of soft decoupling than in those of hard decoupling. This suggests the practical applicability of soft-decoupling techniques in managing stray couplings.

With increasing direct-coupling strength g_{12}, the stray safe zones become wider. This suggests that a nonzero direct coupling between Q_1 and Q_2 can better help to keep the stray-coupling strength small as it may supply a broader range of operational parameters. Similarly to the previous section, in the soft isolated circuits shown in Fig. 7 we demonstrate the ZZ gate on Q_2 and Q_3 can be turned on and off by one tuning the coupler frequency between them, i.e., $\omega_{c_{23}}$; i.e., this gate can be turned on (off) by one increasing (decreasing) $\omega_{c_{23}}$.

To quantify the impact of three-body ZZZ interactions on two-qubit gates, we evaluate the fidelity of the controlled-Z gate between Q_2 and Q_3 for both hard J decoupling and soft J decoupling. For simplicity, we assume there is no decoherence from the qubits to the environment and calculate the maximum fidelity as a function of the coupler frequencies $\omega_{c_{23}}$ at specific coupler frequency $\omega_{c_{13}}$ within the low-error zone. The comparison in Fig. 8 indicates that the ZZZ interaction introduces approximately a 0.2% error, thus excluding the hard-decoupling case beyond the error-correction threshold.

Overall, our comparative analysis with hard decoupling demonstrates that the soft-decoupling scenario can provide equivalent or broader stray-free zones compared with the hard-decoupling scenario. The comparison indicates that higher-level interactions between gated and ungated qubits play a crucial role and require careful management.

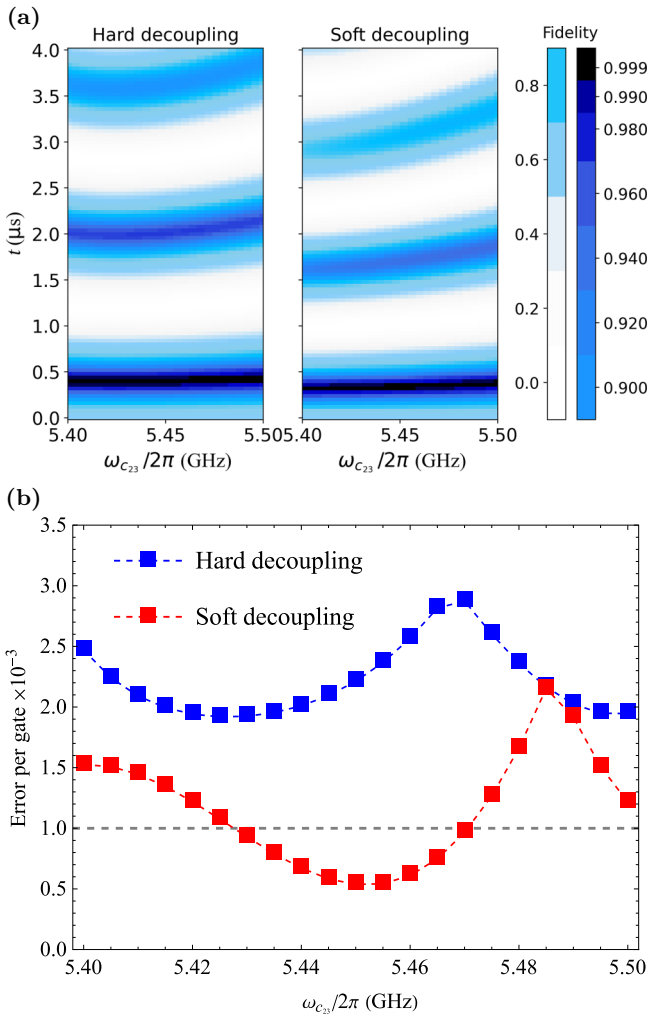

FIG. 8. (a) Controlled-Z-gate fidelity between Q_2 and Q_3 for the cases of hard and soft decoupling as a function of $\omega_{c_{23}}$ and time t. (b) Maximum controlled-Z-gate fidelity as a function of $\omega_{c_{23}}$ for the cases of hard decoupling (blue) and soft decoupling (red).

These characteristics can be encapsulated in the form of ZZZ interactions. In quantum processors, where the fundamental operations are single-qubit and two-qubit gates, these interactions should be carefully suppressed either at the design stage by one reducing connectivity or lowering capacitive coupling, or at the gate stage by one using the soft-decoupling method described above, which involves tuning of circuit parameters such as the coupler frequency to optimize performance and suppress unwanted interactions. By integrating these strategies, we can increase the reliability and efficiency of quantum processors.

V. *ZZZ* SUPERIORITY

We study the two-body and three-body stray interactions in superconducting quantum processors, with a particular focus on scenarios where the strength of three-body ZZZ interactions surpasses that of two-body interactions. This observation would potentially affect the design consideration of future superconducting transmon architectures.

In the circuits described in Sec. IV A, we parameterized the circuits so that Q_1 does not J^{00}-interact with Q_2 and Q_3. We evaluated ZZZ and ZZ strengths in Sec. IV A. We use the data and compute the ratio of $|ZZZ|$ to the maximum two-body interaction strength under different capacitive-coupling strengths between Q_1 and Q_2, e.g., $g_{12}/2\pi = 4$ MHz and $g_{12}/2\pi = 13$ MHz. The results are depicted in Figs. 9(a) and 9(b). While the blue region aligns with the expected hierarchies in MBL theory, the red areas reveal a specific domain of parameters under which three-body interactions exceed two-body interactions, particularly at coupler frequencies close to the qubit frequencies. In these regions, ZZZ interactions become more dominant than two-body interactions for certain coupler frequencies, namely, "ZZZ superiority." In Fig. 9, the "ZZZ-superiority" region is highlighted, with its boundary indicated by a solid green line where $|ZZZ| = |ZZ_{\max}|$. The increase in the prominence of three-body interactions with stronger direct coupling is a noteworthy observation.

The circles labeled A–F in Figs. 9(a) and 9(b) represent three sweet spots for the OFF-OFF-ON gate studied in Fig. 6. The analysis indicates that certain ON spots that are near the three-body superiority zone, such as point A, are not ideal as a safe gate sweet spot. In such operational points, while ZZ strengths are small, the three-body ZZZ interaction can exceed ZZ interactions, which can lead to noisy gate operations. Figures 9(c) and 9(d) show the behavior of stray couplings at the fixed frequency $\omega_{c_{23}}/2\pi = 5.272$ GHz, represented by a dashed white line in Figs. 9(a) and 9(b). The behavior is examined across a range of $\omega_{c_{23}}$ frequencies for both weak and strong g_{12}. In the weak-direct-coupling g_{12} case, a narrow band around $\omega_{c_{13}}/2\pi = 6$ GHz can be identified in which all residual stray interactions are small. This observation indicates that the specified frequency range may act as a zone with minimal error, which is optimal for establishing a quantum idle point. Consequently, this parameter domain is suitable for implementing a controlled-Z gate between Q_2 and Q_3. Another example of a three-qubit circuit, where three qubits are coupled to a shared coupler, is provided in Appendix F.

This analysis highlights the intricate balance of multiqubit interactions in quantum circuits, emphasizing the need to consider both two-body and three-body interactions in circuit design. Especially in scenarios aiming for high-fidelity gate operations, the findings suggest that a nuanced understanding of these interactions can lead to optimized strategies for quantum computing. This approach avoids oversimplified assumptions of interaction hierarchies and paves the way for more-effective quantum gate designs.

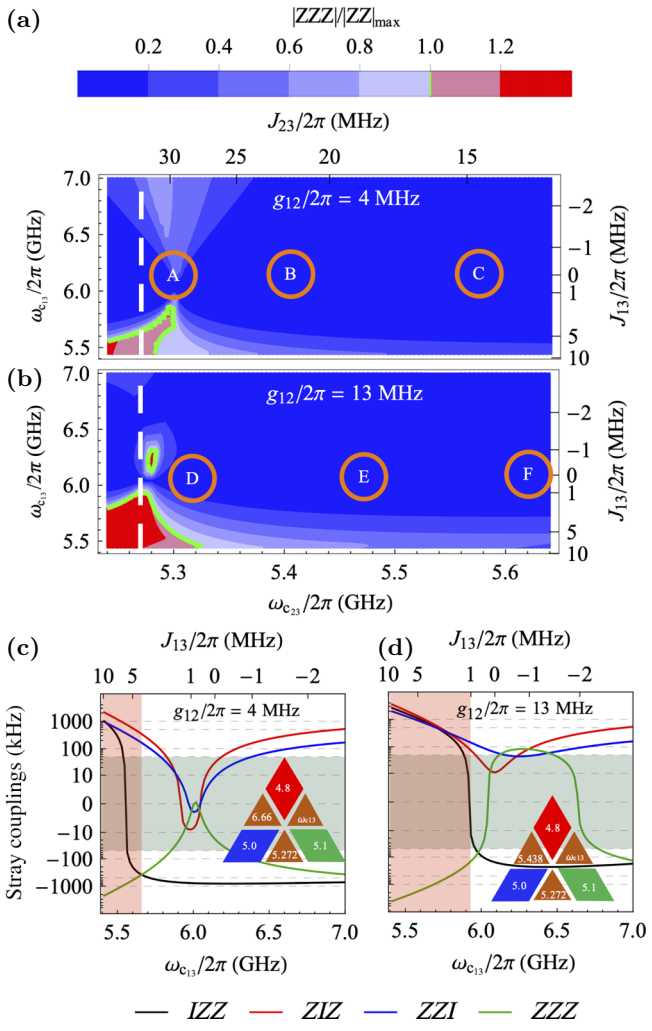

FIG. 9. Absolute ratio of the three-body *ZZZ* interaction and the maximum of the two-body interactions occurring in the triangular circuit in Fig. 3 as a function of the frequencies of the resonators C_{23} and C_{13}, $\omega_{c_{23}}$ and $\omega_{c_{13}}$, at (a) $g_{12}/2\pi =$ 4 MHz and (b) $g_{12}/2\pi = 13$ MHz, respectively. The green contour line represents $|\alpha_{ZZZ}| = \max(|\alpha_{Z_iZ_jI_k}|)$. Corresponding stray couplings at specific coupler frequency $\omega_{c_{23}}/2\pi = 5.272$ GHz [dashed white line in (a),(b)] are shown in (c),(d), respectively. The gray area indicates stray couplings are less than 50 kHz, and the light-green area shows the validity of *ZZZ* superiority. Other circuit parameters are the same as in Fig. 4 with $\omega_2/2\pi =$ 5.0 GHz.

VI. CROSS-RESONANCE GATE ON A LATTICE

A cross-resonance (CR) gate is a type of interacting entanglement between two qubits, applied locally on one qubit, namely, "control," and makes the other qubit, namely, "target," undergo a $\pm\hat{X}$ operation, with $\pm$ being subject to the state of the control qubit; i.e., the interacting Hamiltonian between is *ZX*. This can be done in the laboratory by one driving the control qubit with a microwave pulse of frequency of the target qubit [50,51]. Here we study the impact of microwave driving on the strength of stray couplings.

Application of a CR gate on qubits has an impact on the stray couplings between qubits, and this was extensively studied in Refs. [45,52–54]. In Refs. [45,55,56] it was proposed that the microwave-activated part of the stray coupling could occur with the opposite sign of the static stray coupling of no CR gate, so by tuning the circuit parameters, one can cancel the two and make so-called *ZZ*-free qubits, which is yet to be verified experimentally. However, the detailed impact of a CR gate on the lattice Hamilton in the many-body form is unknown.

In this section, we study the impact of a CR gate on *ZZ* and *ZZZ* interactions for a system of superconducting qubits. The microwave driving Hamiltonian in the laboratory frame is $H_{\text{drive}} = \Omega\cos(\omega_{\text{target}}t)(\hat{a}_{\text{control}} + \hat{a}^{\dagger}_{\text{control}})$. We take this part of the Hamiltonian into the relevant frame of nonperturbative block diagonalization, and together with the static Hamiltonian in the basis of $|Q_{\text{control}}, Q_{\text{target}}, Q_{\text{spectator}}\rangle$, the final result has the following general form:

$$H = \alpha_{ZZI}\frac{ZZI}{4} + \alpha_{ZIZ}\frac{ZIZ}{4} + \alpha_{IZZ}\frac{IZZ}{4} + \alpha_{ZZZ}\frac{ZZZ}{8} + \alpha_{ZXI}\frac{ZXI}{2} + \alpha_{ZXZ}\frac{ZXZ}{4}. \tag{12}$$

Here classical crosstalk is assumed to be canceled. The two-qubit version of these Pauli coefficients—α_{ijk} with one of the three indices being the identity and the other two from the set $\{I, Z, X, Y\}$—were analytically determined by perturbative block-diagonalization techniques in Refs. [45,47]. Nonperturbative numerical analysis shows that the pairwise Pauli coefficients in the leading order of the CR-gate amplitude scale as $\alpha_{ZZ}(\Omega) = \alpha_{ZZ}(0) + \eta_2\Omega^2 + \eta_a\Omega^a$, with coupler frequency–dependent power $4 \le a \le 5$, and $\alpha_{ZX}(\Omega) = \mu_1\Omega + \mu_b\Omega^b$, with b being nearly 3. For more discussion on the method of evaluation and the domain of parameters, see Fig. 8 in Ref. [54]. It is evident that *ZZZ* interaction under the microwave drive of a CR gate changes from its static value by the following form, which can be verified perturbatively: $\alpha_{ZZZ}(\Omega) = \alpha_{ZZZ}(0) + \nu_2\Omega^2 + O(3)$ in the leading order, where ν_2 depends on the parameters of the circuit and can be positive or negative, meaning that the microwave-activated part of the *ZZZ* interaction can add or reduce error from the circuit lattice Hamiltonian.

We evaluate the Pauli coefficients in the lattice Hamiltonian of Eq. (12) numerically. To compare our simulation results with experimental results, we study the recent measurement data of a seven-qubit circuit in Ref. [6], as shown in Fig. 10. Qubits interact by a cross-resonance gate. In particular, Cai *et al.* [6] assess spectator errors through three-qubit tomography in Fig. S7(D). In this case, let Q_2

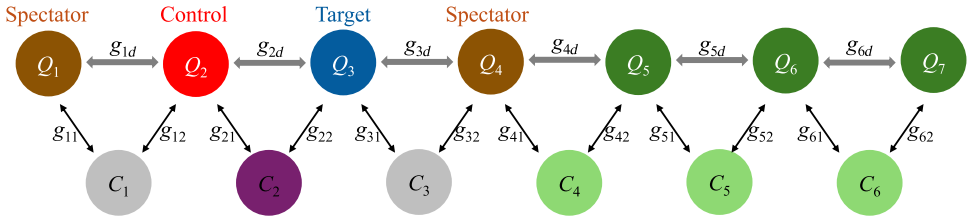

FIG. 10. Thirteen Xmon qubits, with the bottom six qubits serving as tunable couplers. See Ref. [6] for more details.

be the control qubit, Q_3 the target, and Q_4 the target spectator qubit, with no coupler between Q_2 and Q_4. Here we use our nonperturbative approach to simulate the corresponding Pauli coefficients at the driving amplitude $\Omega/2\pi = 18$ MHz, illustrated in Fig. 11. To match the measured *ZZZ* and *ZXZ* data, we assume Q_2 and Q_4 are capacitively coupled with strength $g_{24d}/2\pi = 4.5$ MHz. Markers depict the extracted experimental data, while curves represent results from our numerical method. Our theory effectively predicts the behavior of such qubit-chain devices.

Table I summarizes several static and microwave-activated resonances—perturbative divergences—caused by the presence of a third qubit in the circuit, as discussed in Ref. [6]. The static (microwave-activated) resonances are highlighted by vertical dashed blue (black) lines in Fig. 4. The introduction of a third qubit leads to numerous higher-level divergences that are not accounted for in the two-qubit analysis.

To further our understanding of the impact of a CR gate on the lattice Hamiltonian of three qubits, we use CirQubit to generate numerical data for the cases where experiments have not been conducted, such as the static stray coupling in the absence of a CR gate, $\Omega = 0$, and the case of the CR-gate amplitude Ω being 31 MHz, which is almost double the experimental value of 16 MHz. Results are plotted in Fig. 21 in Appendix G, which indicates how the lattice Pauli coefficients of Eq. (12) depend on the frequency detuning between control and target qubits Δ_{st}. Interestingly, we see in Fig. 21 in a large domain of Δ_{st} that by one increasing the microwave power, the *ZXI* and *ZXZ* interactions become stronger, while *ZZ* and *ZZZ* stray couplings are suppressed. The suppression of *ZZ* stray couplings was predicted in Ref. [45], and is known as "*ZZ* freedom." Here we extend that result by demonstrating that it is possible to

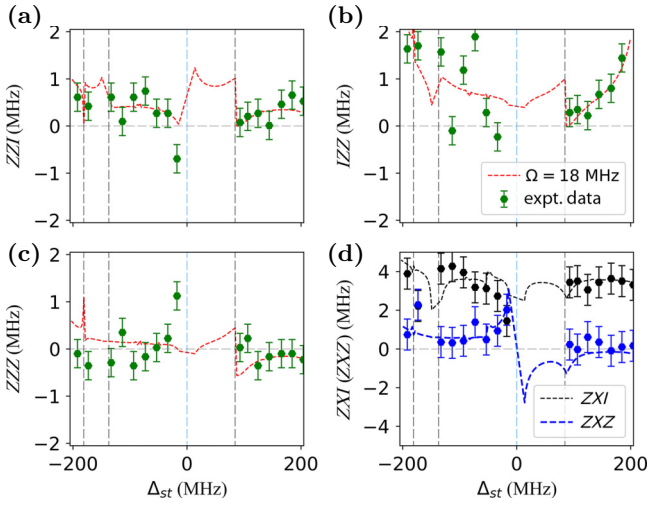

FIG. 11. Interaction terms with varying spectator-target detuning Δ_{st} with fixed CR drive amplitude $\Omega/2\pi = 18$ MHz when considering parasitic interactions from the target spectator qubit: (a) *ZZI*, (b) *IZZ*, (c) *ZZZ*, and (d) *ZXI* (*ZXZ*). Markers represent the extracted experimental data in Ref. [6], and curves represent the numerical simulation results.

TABLE I. Summary of three-qubit resonances in the three-qubit subspace. The states are denoted in the following order: $|Q_{\text{control}}Q_{\text{target}}Q_{\text{spectator}}\rangle$ and "$\sim$" means the in resonance takes place between the two states. The circuit parameters are the same as in Fig. 4.

Resonances	Condition	$\frac{\Delta_{st}}{2\pi}$ (MHz)
Static resonances		
$\|001\rangle \sim \|010\rangle$	$\Delta_{st} = 0$	0
$\|101\rangle \sim \|110\rangle$		
$\|001\rangle \sim \|100\rangle$	$\Delta_{cs} = 0$	137
$\|011\rangle \sim \|110\rangle$		
$\|011\rangle \sim \|020\rangle$	$\Delta_{st} = \delta_2$	−218
$\|111\rangle \sim \|120\rangle$		
$\|011\rangle \sim \|002\rangle$	$\Delta_{st} = -\delta_3$	213
$\|111\rangle \sim \|102\rangle$		
$\|011\rangle \sim \|200\rangle$	$\Delta_{cs} + \Delta_{cs} = -\delta_1$	56
$\|101\rangle \sim \|200\rangle$	$\Delta_{cs} = -\delta_1$	−81
$\|111\rangle \sim \|210\rangle$		
$\|101\rangle \sim \|002\rangle$	$\Delta_{cs} = \delta_3$	350
$\|111\rangle \sim \|012\rangle$		
$\|101\rangle \sim \|020\rangle$	$\Delta_{ct} + \Delta_{st} = \delta_2$	−355
$\|110\rangle \sim \|002\rangle$	$\Delta_{cs} - \Delta_{st} = \delta_3$	175
$\|020\rangle \sim \|002\rangle$	$2\Delta_{st} = \delta_2 - \delta_3$	−2.5
$\|200\rangle \sim \|002\rangle$	$2\Delta_{st} - 2\Delta_{ct} = \delta_1 - \delta_3$	134.5
$\|012\rangle \sim \|120\rangle$	$2\Delta_{st} = \Delta_{ct} + \delta_2 - \delta_3$	66
CR-activated resonances		
$\|000\rangle\|n_d + 2\rangle \sim \|002\rangle\|n_d\rangle$	$2\Delta_{st} = -\delta_3$	106.5
$\|000\rangle\|n_d + 2\rangle \sim \|101\rangle\|n_d\rangle$	$\Delta_{st} = -\Delta_{ct}$	−137
$\|300\rangle\|n_d + 1\rangle \sim \|202\rangle\|n_d\rangle$	$2\Delta_{st} = \Delta_{ct} + 2\delta_1 - \delta_3$	−180
$\|003\rangle\|n_d + 1\rangle \sim \|400\rangle\|n_d\rangle$	$3\Delta_{st} = 4\Delta_{ct} + 6\delta_1 - 3\delta_3$	−40.3

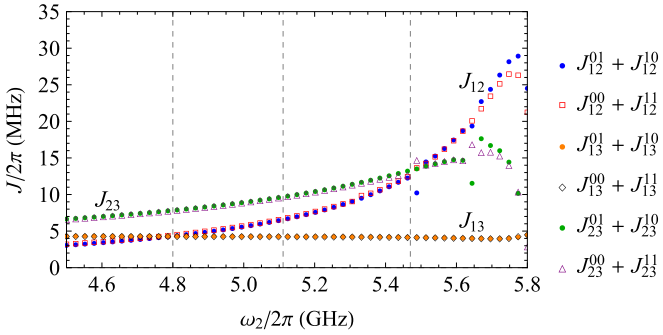

FIG. 12. Numerical simulation of J relations in Eq. (4). The circuit parameters are the same as those in Fig. 4.

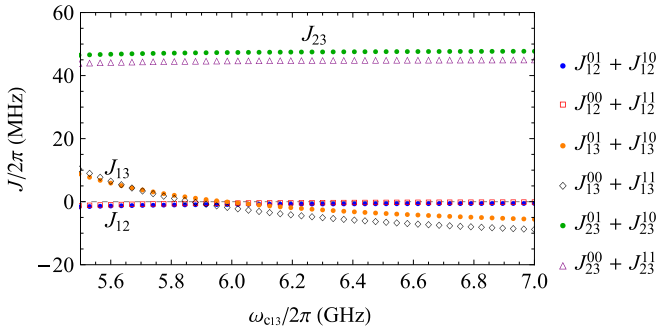

FIG. 13. Numerical simulation of J relations in Eq. (4). The circuit parameters are the same as those in Fig. 9(c).

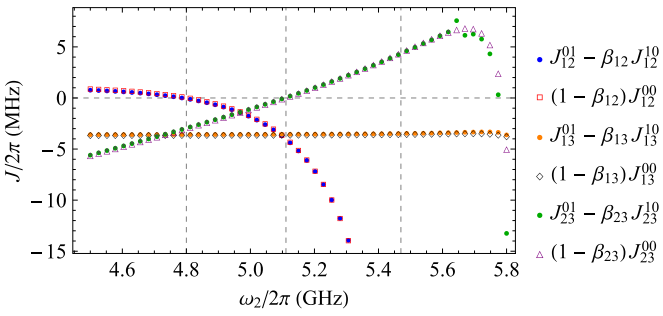

FIG. 14. Numerical simulation of J relations in Eq. (11). The circuit parameters are the same as those in Fig. 4.

tune the circuit parameters to suppress the three-body stray coupling ZZZ.

VII. CONCLUSION

In conclusion, this study underscores the critical importance of considering the lattice Hamiltonian and many-body couplings in the design and operation of quantum circuits. This approach allows fine-tuning of circuit parameters to mitigate the detrimental effects of stray couplings. Furthermore, we demonstrate that three-body stray couplings can be as significant as two-body interactions, particularly beyond the dispersive regime. Effectively controlling these interactions through strategic adjustments

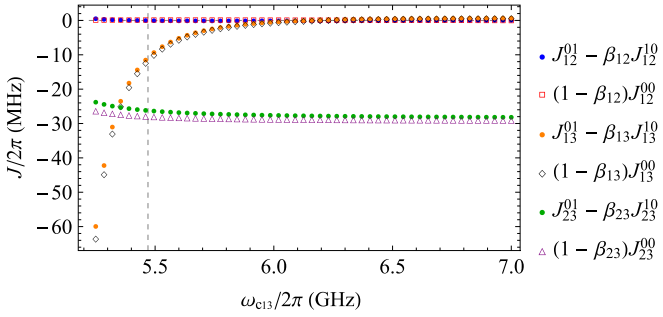

FIG. 15. Numerical simulation of J relations in Eq. (11). The circuit parameters are the same as those in Fig. 9(c).

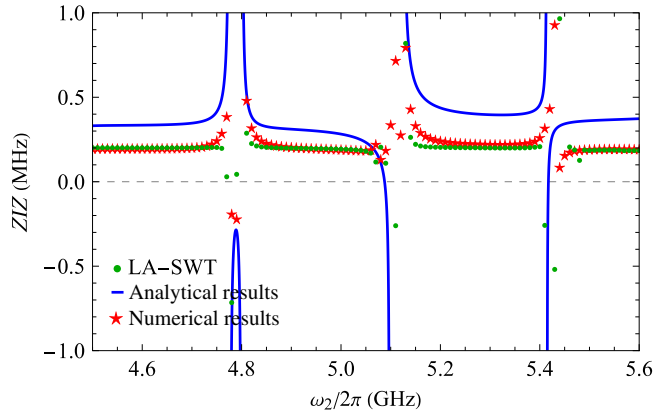

FIG. 16. Least-action (LA)–SWT approach versus the analytical formula and the numerical method. The green dots represent the LA-SWT results. The circuit parameters are same as in Fig. 4.

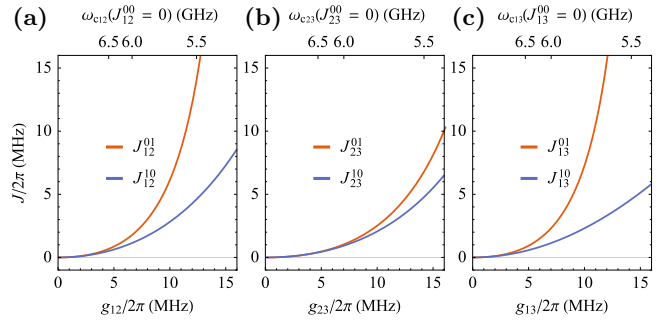

FIG. 17. Effective-qubit-qubit-coupling discrepancy from analytical simulation. (a) J_{12}^{01} and J_{12}^{10} as a function of direct coupling g_{12} when J_{12}^{00} is OFF. (b) J_{13}^{01} and J_{13}^{10} as a function of direct coupling g_{13} when J_{13}^{00} is OFF. (c) J_{23}^{01} and J_{23}^{10} as a function of direct coupling g_{23} when J_{23}^{00} is OFF. The corresponding coupler frequency is given at the top of each plot.

can enhance gate performance and holds potential for the implementation of high-fidelity two-qubit gates.

Additionally, we have shown that the dominance of three-body ZZZ interactions can be realized within the quasidispersive regime, suggesting the possibility of achieving optimal quantum performance even outside the

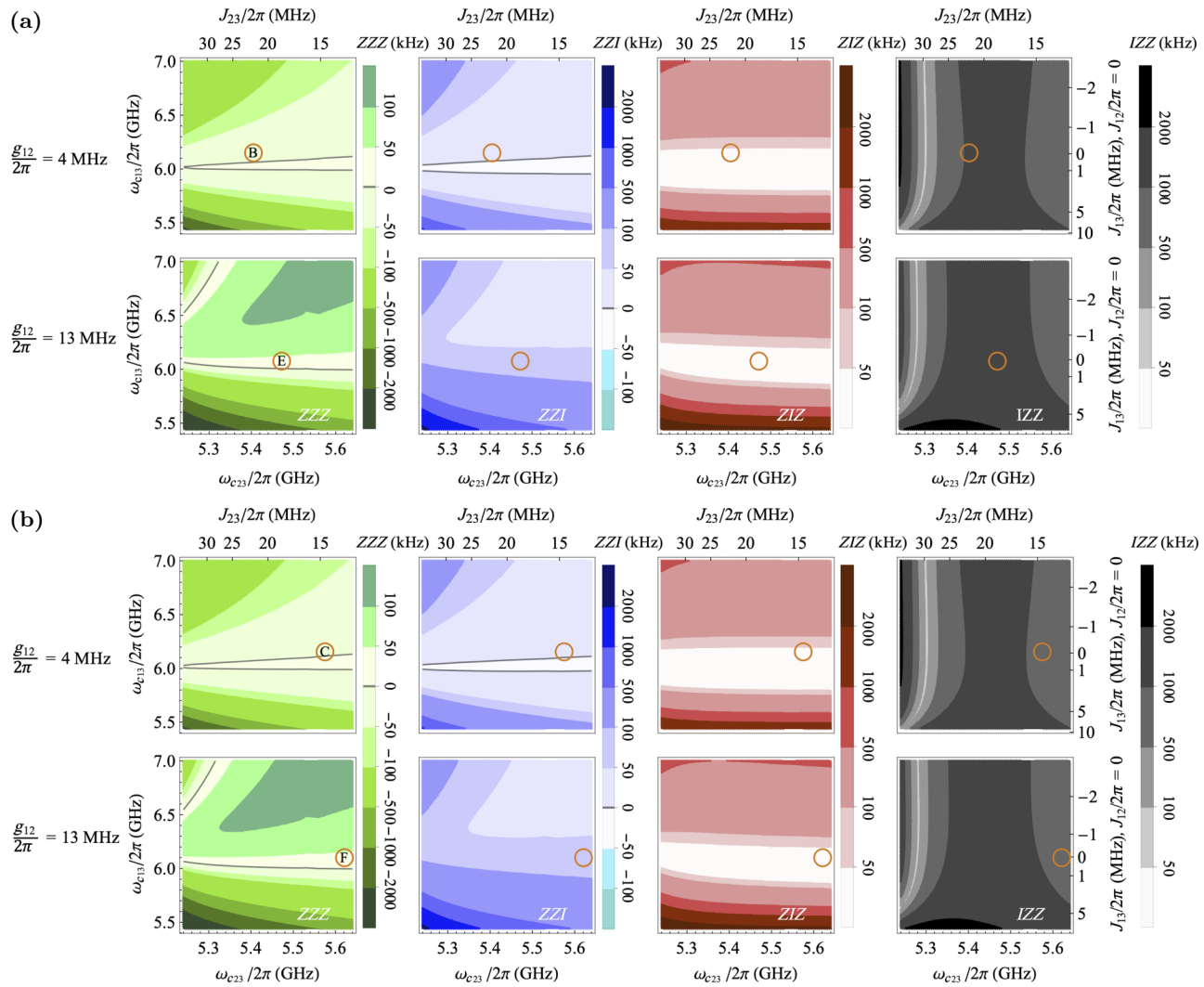

FIG. 18. (a) Stray couplings in the triangular circuit with all-to-all connectivity as a function of the frequencies of the resonators C_{13} and C_{23}, $\omega_{c_{13}}$ and $\omega_{c_{23}}$, respectively. The first row is at $g_{12}/2\pi = 4$ MHz with nearly zero J_{12} and J_{13} at point B: $(\omega_{c_{12}}/2\pi, \omega_{c_{23}}/2\pi, \omega_{c_{13}}/2\pi) = (6.67, 5.405, 6.15)$ GHz. The second row is at $g_{12}/2\pi = 13$ MHz with nearly zero J_{12} and J_{13} at point E: $(\omega_{c_{12}}/2\pi, \omega_{c_{23}}/2\pi, \omega_{c_{13}}/2\pi) = (5.443, 5.472, 6.076)$ GHz. (b) The first (second) row is at $g_{12}/2\pi = 4$ MHz ($g_{12}/2\pi = 13$ MHz) with nearly zero J_{12} and J_{13} at point C: $(\omega_{c_{12}}/2\pi, \omega_{c_{23}}/2\pi, \omega_{c_{13}}/2\pi) = (6.68, 5.275, 6.154)$ GHz. In the second row J_{12} and J_{13} are nearly zero at point F: $(\omega_{c_{12}}/2\pi, \omega_{c_{23}}/2\pi, \omega_{c_{13}}/2\pi) = (5.446, 5.621, 6.098)$ GHz. Other circuit parameters are the same as in Fig. 4 with $\omega_2/2\pi = 5.0$ GHz.

near-degenerate regimes. These findings offer significant contributions to the fields of quantum system design and algorithm optimization, promising increases in the efficiency and robustness of quantum computing technologies.

ACKNOWLEDGMENTS

M.H.A. expresses gratitude for technical support by and enriching discussions with Joséphine Pazem that greatly contributed to the development of this work. X.X. was partially supported by the project GeQCoS (Grant No. 13N15685). Manabputra's involvement was partially supported by the Kishore Vaigyanik Protsahan Yojana program, sponsored by the Department of Science and Technology, Government of India. This research received funding from the Horizon Europe project OpenSuperQ-Plus100 (Grant Agreement No. 101113946).

APPENDIX A: PERTURBATIVE *ZZ* AND *ZZZ* ON A TRIANGULAR LATTICE

The explicit formulas for stray couplings, derived from perturbation theory, are presented below:

$$\alpha_{ZZI} = \frac{2\left(J_{12}^{01}\right)^2}{\Delta_{12}^{01}} - \frac{2\left(J_{12}^{10}\right)^2}{\Delta_{12}^{10}} + \frac{4J_{12}^{00}J_{23}^{00}J_{13}^{00}}{\Delta_{23}^{00}\Delta_{13}^{00}}$$

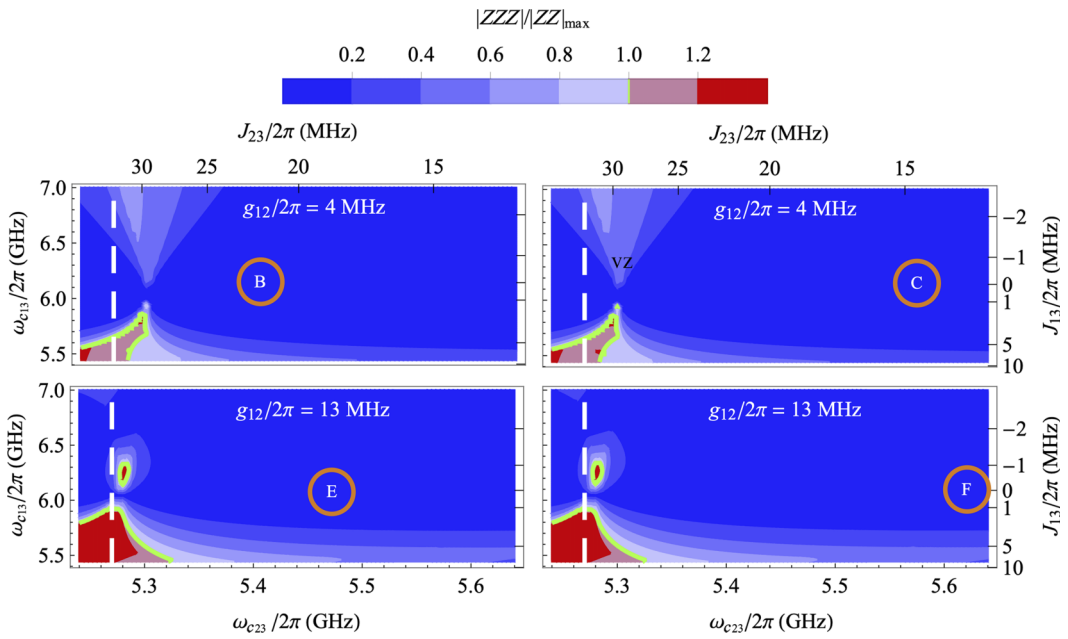

FIG. 19. Absolute ratio of the three-body ZZZ interaction and the maximum of the two-body interactions occurring in the triangular circuit as a function of the frequencies of the resonators C_{23} and C_{13}, ω_{c23} and ω_{c13}, at $g_{12}/2\pi = 4$ MHz with points B and C in the first row and $g_{12}/2\pi = 13$ MHz with points E and F in the second row, respectively. Other circuit parameters are the same as in Fig. 4 with $\omega_2/2\pi = 5.0$ GHz.

$$+4\left(\frac{J_{12}^{00}J_{23}^{01}J_{13}^{01}}{\Delta_{23}^{01}\Delta_{13}^{01}}-\frac{J_{13}^{00}J_{12}^{01}J_{23}^{10}}{\Delta_{23}^{10}\Delta_{13}^{00}}-\frac{J_{23}^{00}J_{13}^{10}J_{12}^{10}}{\Delta_{13}^{10}\Delta_{23}^{00}}-\frac{J_{13}^{11}J_{23}^{01}J_{12}^{10}}{\Delta_{23}^{01}\Delta_{12}^{10}}+\frac{J_{23}^{11}J_{12}^{01}J_{13}^{01}}{\Delta_{12}^{01}\Delta_{13}^{01}}+\frac{J_{12}^{11}J_{13}^{10}J_{23}^{10}}{\Delta_{13}^{10}\Delta_{23}^{10}}\right), \quad \text{(A1)}$$

$$\alpha_{ZIZ}=\frac{2\left(J_{13}^{01}\right)^2}{\Delta_{13}^{01}}-\frac{2\left(J_{13}^{10}\right)^2}{\Delta_{13}^{10}}+\frac{4J_{13}^{00}J_{23}^{00}J_{12}^{00}}{\Delta_{23}^{00}\Delta_{12}^{00}}+4\left(-\frac{J_{13}^{00}J_{12}^{01}J_{23}^{10}}{\Delta_{12}^{01}\Delta_{23}^{10}}+\frac{J_{12}^{00}J_{23}^{01}J_{13}^{01}}{\Delta_{12}^{00}\Delta_{23}^{01}}+\frac{J_{23}^{00}J_{13}^{10}J_{12}^{10}}{\Delta_{23}^{00}\Delta_{12}^{10}}-\frac{J_{13}^{11}J_{23}^{01}J_{12}^{10}}{\Delta_{23}^{01}\Delta_{12}^{10}}+\frac{J_{23}^{11}J_{12}^{01}J_{13}^{01}}{\Delta_{12}^{01}\Delta_{13}^{01}}+\frac{J_{12}^{11}J_{13}^{10}J_{23}^{10}}{\Delta_{13}^{10}\Delta_{23}^{10}}\right), \quad \text{(A2)}$$

$$\alpha_{IZZ}=\frac{2\left(J_{23}^{01}\right)^2}{\Delta_{23}^{01}}-\frac{2\left(J_{23}^{10}\right)^2}{\Delta_{23}^{10}}+\frac{4J_{23}^{00}J_{13}^{00}J_{12}^{00}}{\Delta_{13}^{00}\Delta_{12}^{00}}+4\left(\frac{J_{23}^{00}J_{12}^{10}J_{13}^{10}}{\Delta_{12}^{10}\Delta_{13}^{10}}-\frac{J_{12}^{00}J_{23}^{01}J_{13}^{01}}{\Delta_{12}^{00}\Delta_{13}^{01}}-\frac{J_{13}^{00}J_{23}^{10}J_{12}^{01}}{\Delta_{13}^{00}\Delta_{12}^{10}}-\frac{J_{13}^{11}J_{23}^{01}J_{12}^{10}}{\Delta_{23}^{01}\Delta_{12}^{10}}+\frac{J_{23}^{11}J_{12}^{01}J_{13}^{01}}{\Delta_{12}^{01}\Delta_{13}^{01}}+\frac{J_{12}^{11}J_{13}^{10}J_{23}^{10}}{\Delta_{13}^{10}\Delta_{23}^{10}}\right), \quad \text{(A3)}$$

$$\alpha_{ZZZ}=8\left(\frac{J_{13}^{00}J_{23}^{10}J_{12}^{01}}{\Delta_{23}^{10}\Delta_{12}^{01}}-\frac{J_{12}^{00}J_{13}^{01}J_{23}^{01}}{\Delta_{23}^{01}\Delta_{13}^{01}}-\frac{J_{23}^{00}J_{12}^{10}J_{13}^{10}}{\Delta_{12}^{10}\Delta_{13}^{10}}+\frac{J_{13}^{11}J_{23}^{01}J_{12}^{10}}{\Delta_{23}^{01}\Delta_{12}^{10}}-\frac{J_{23}^{11}J_{12}^{01}J_{13}^{01}}{\Delta_{12}^{01}\Delta_{13}^{01}}-\frac{J_{12}^{11}J_{13}^{10}J_{23}^{10}}{\Delta_{13}^{10}\Delta_{23}^{10}}\right). \quad \text{(A4)}$$

APPENDIX B: REDUCED-CIRCUIT HAMILTONIAN

To derive the analytical formulas given in Eqs. (3)–(6), we start from the Hamiltonian in Eq. (7), which describes the circuit in Fig. 3 with three qubits coupled to one another by three couplers. We use the rotating-wave approximation and ignore the fast oscillating terms in the Hamiltonian to get the new Hamiltonian as

$$\frac{H}{\hbar}=\sum_{r=1}^{3}\omega_{c_r}c_r^{\dagger}c_r+\sum_{q=1}^{3}\sum_{n_q}\omega_{n_q}|n_q\rangle\langle n_q| +\sum_{r=1}^{3}\sum_{q=1}^{3}g_{qc_r}(c_r a_q^{\dagger}-c_r^{\dagger}a_q) +\sum_{q\neq q'}^{3}\sum_{q'=1}^{3}g_{qq'}(a_q a_{q'}^{\dagger}-a_q^{\dagger}a_{q'}). \quad \text{(B1)}$$

Using the first order Schrieffer–Wolff transformation, we block-diagonalize the Hamiltonian to decouple the couplers from the qubits. The only qubit Hamiltonian thus obtained is as follows:

$$\frac{H_s}{\hbar}=\sum_{q=1}^{3}\sum_{n_q}\tilde{\omega}_{n_q}|n_q\rangle\langle n_q|+\sum_{q\neq q'}\sum_{n_q,m_{q'}}\sqrt{n_q+1}\sqrt{m_{q'}+1} +J_{qq'}^{n_q m_{q'}}(|n_q+1,m_{q'}\rangle\langle n_q,m_{q'}+1|+\text{H.c.}). \quad \text{(B2)}$$

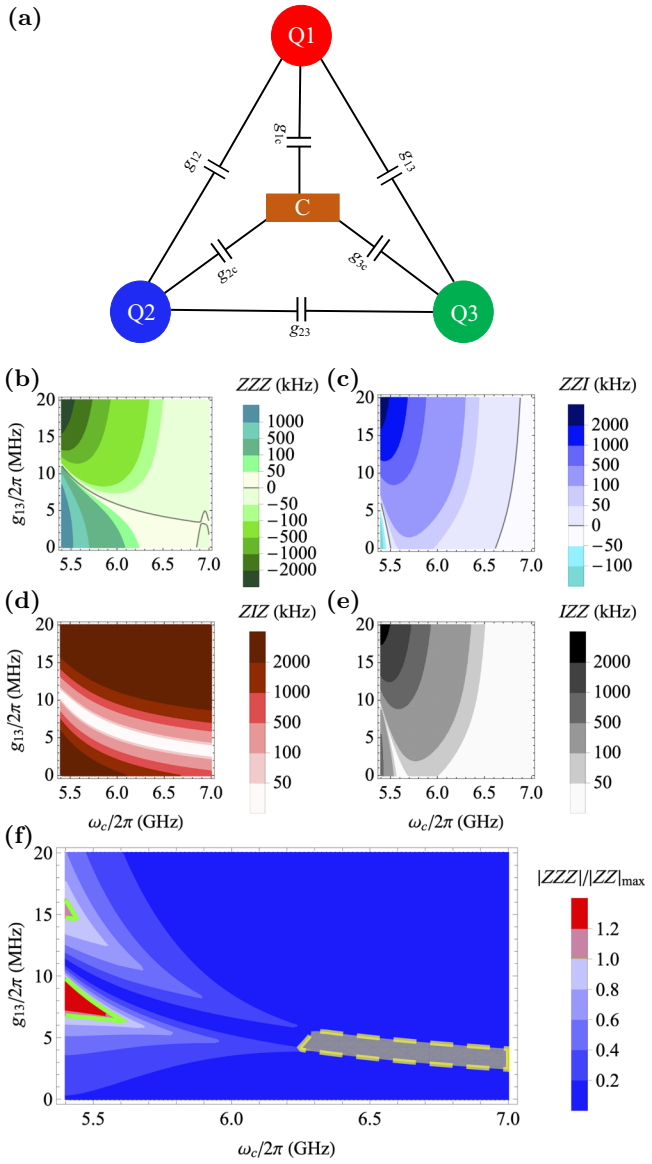

FIG. 20. (a) Triangle geometry of three-qubit interaction indirectly coupled via one shared coupler. Stray couplings versus coupler frequency of the circuit: (b) ZZZ, (c) ZZI, (d) ZIZ, (e) IZZ, and (f) $|ZZZ|/|ZZ|_{\max}$. The circuit parameters are $\omega_1/2\pi = 4.8$ GHz, $\omega_2/2\pi = 5.0$ GHz, $\omega_3/2\pi = 5.1$ GHz, $\delta_1/2\pi = \delta_2/2\pi = \delta_3/2\pi = -330$ MHz with qubit-coupler strength $g_{1c_1}/2\pi = g_{1c_3}/2\pi = g_{2c_1}/2\pi = g_{3c_3}/2\pi = 85$ MHz and $g_{2c_2}/2\pi = g_{3c_2}/2\pi = 102$ MHz, and direct qubit-qubit coupling $g_{12} = g_{23}/2\pi = 4$ MHz.

We then restrict this Hamiltonian to the computational subspace and fully diagonalize it using the Schrieffer–Wolff transformation to the third order and rewrite it in the Pauli basis as in Eq. (2) with the coefficients given by Eqs. (3)–(6).

APPENDIX C: QUBIT COUPLING SYMMETRY

In the main text, we presented a number of identities for the effective J coupling strength between qubits, Eqs. (4) and (11). These relations can be proven with use of the perturbative definition of the coupling, Eq. (10).

It is interesting to numerically verify these identities beyond the dispersive regime as well, and one way to do this is to numerically evaluate the two sides of the identities (4) and (11) and verify their overlap. For this purpose, we simulate the J relations using the nonperturbative approach with the circuit parameters similar to those in Fig. 4. The results are shown in Fig. 12. We conduct a comparative analysis between the sums $J_{ij}^{01} + J_{ij}^{10}$ and $J_{ij}^{00} + J_{ij}^{11}$ to illustrate that in the dispersive regime, characterized by $J/\Delta \ll 1$, the relationship approximated by Eq. (4) holds. However, as the frequency of an individual qubit, such as Q_2, approaches the vicinity of the couplers, a noticeable divergence emerges between the two sums. Another illustrative example, with circuit parameters identical to those in Fig. 9(c), demonstrates analogous results, as depicted in Fig. 13.

Figures 14 and 15 depict the numerical simulation of Eq. (11) using parameters similar to those in Figs. 4 and 9(c), respectively. These results exhibit significant consistency, affirming the validity of the identity.

APPENDIX D: *ZIZ* DISCREPANCY

Instead of relying on a perturbative block-diagonalization technique such as the Schrieffer-Wolff transformation, which is primarily accurate in the dispersive regime, an alternative approach can be used to achieve exact multi-block-diagonalization, when analytical expressions are not required. This technique is called the "least-action method" [47,48], and aims to identify the block-diagonal Hamiltonian that exhibits the highest degree of similarity to the true Hamiltonian, as governed by the principle of least action. By using this precise approach to decouple the couplers from the qubits, our analysis encompasses the higher-order interactions, as it is an exact method. Subsequently, the Schrieffer-Wolff transformation can be used to fully diagonalize the qubit Hamiltonian. On comparing the results obtained with this approach, as shown in Fig. 16, with the ZIZ interaction depicted in Fig. 4(b), it becomes evident that the former approach exhibits greater accuracy than the numerical simulation.

This observation indicates that the discrepancy in the ZIZ interaction arises primarily from the initial Schrieffer-Wolff transformation. This is likely attributed to the fact that the effective interaction strength between two qubits, denoted as J_{ij}^{mn} and derived with use of the SWT, does not incorporate any higher-order contributions from the third qubit in the circuit. However, these effects are accurately captured through the numerical simulation and the least-action method.

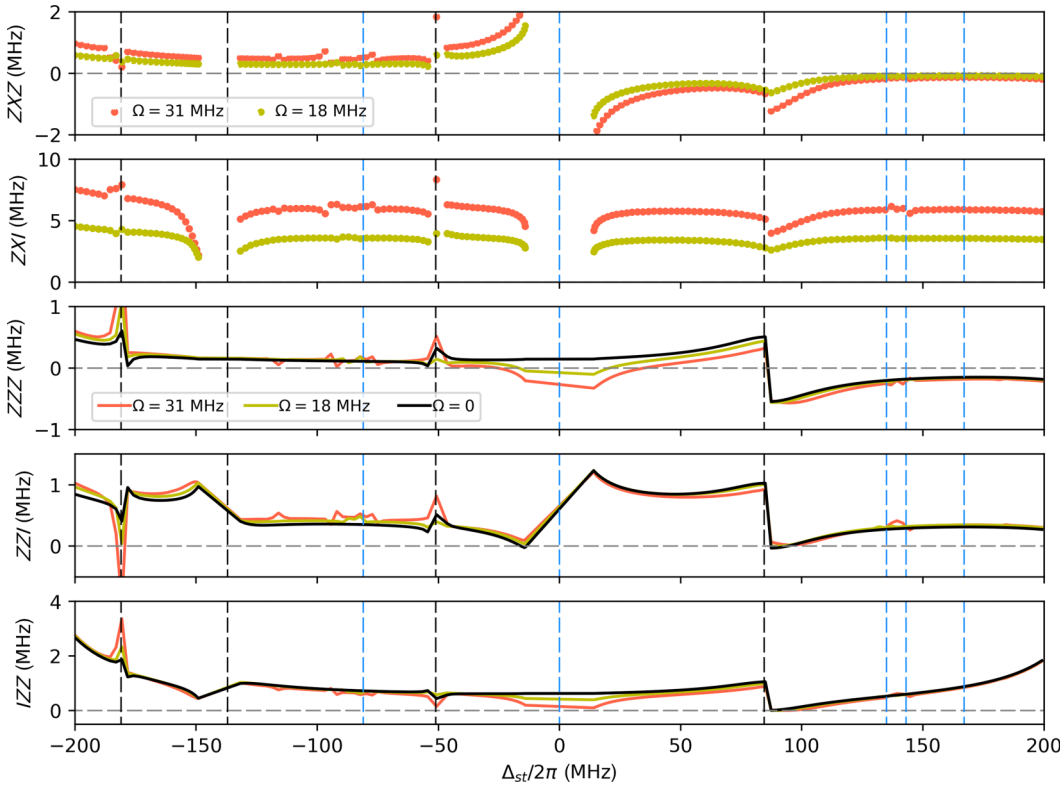

FIG. 21. Pauli CR coefficients at three different driving amplitudes: $\Omega = 0$ (black), $\Omega = 18$ MHz (yellow), and $\Omega = 31$ MHz (pink).

APPENDIX E: EFFECTIVE COUPLING DISCREPANCY

Even when the effective qubit-qubit coupling strength at the lowest order J_{12}^{00} is zero, the qubits are still not necessarily fully decoupled. We can see the effect of this in Fig. 6. Because of the nonlinearity of the superconducting qubits, higher-order interactions may still exist. Figure 17 depicts how the higher-order interaction strengths J^{01} and J^{10} deviate from zero by several megahertz as the direct coupling between the qubits gets stronger or when the couplers are tuned closer to the qubits. As a result, parasitic interactions can still exist between these qubits and need to be accounted for.

In Fig. 18(a), we describe the landscape with C_{12} frequency at decoupling points B and E. In Fig. 18(b), we describe the landscape with C_{12} frequency at decoupling points C and F. Because of the higher-order J^{01} and J^{10} interactions, the landscapes have significant features. In the case of the ZZZ interaction, especially when the qubits are strongly coupled, it can go upwards of a 1000 kHz as $\omega_{c_{23}}$ varies, even when J_{12} is zero. IZZ interaction also varies significantly with $\omega_{c_{23}}$, but ZIZ interaction has little dependence on it. In the second row of graphs, when the direct coupling g_{12} is stronger, the zeroness of ZZI interaction disappears and becomes narrower for ZIZ interaction. At the decoupling points, ZZZ, ZZI, and ZIZ interactions are all smaller than 50 kHz, whereas IZZ interaction is significantly stronger.

In Fig. 19, we plot the ratio of the ZZZ interaction and the maximum of ZZ interactions as we vary the coupler frequencies. The plots on the left have C_{12} frequency at decoupling points B and E, whereas the plots on the right have C_{12} frequency at decoupling points C and F. We see that the ZZZ interaction is stronger than all the ZZ interactions when the couplers are tuned closer to the qubits.

APPENDIX F: THREE QUBITS AND ONE COUPLER

We extend our investigation beyond the case of the three-qubit, three-coupler architecture. In this appendix, we study the case of three qubits sharing a coupler, which resembles the one recently studied in Ref. [27]. For simplicity, we consider three transmon qubits coupled to a harmonic oscillator as the shared coupler, as depicted in Fig. 20(a). Our study aims to examine the behavior of such a system in response to changes in the coupler frequency ω_c and direct coupling, i.e., g_{13}. We present the findings in Fig. 20.

Compared with the triangular circuit depicted in Fig. 3, our analysis reveals that when the coupler frequency

is detuned far away from the qubits, all four stray couplings are effectively suppressed to below 50 kHz at a certain direct coupling g_{13}. As expected, the *ZIZ* coupling is the most influenced by g_{13}, while all other couplings remain almost constant at high coupler frequency, and undergo significant magnitude changes at weak coupler frequencies, where the qubit basis becomes hybridized with the coupler subspace. Additionally, we evaluate the ratio of *ZZZ* interaction to the maximum *ZZ* interaction and observe that *ZZZ* superiority can still be achieved at lower coupler frequencies.

APPENDIX G: CROSS RESONANCE GATE SIMULATION

We study the impact of a CR gate on the lattice Hamiltonian of three qubits as shown in Fig. 10. For this aim we use CirQubit to generate numerical data for the cases for which experiments have not been conducted, such as static stray coupling in the absence of a CR gate, $\Omega = 0$, and the case of the CR-gate amplitude Ω being 31 MHz, which is almost double the experimental value of 16 MHz. Results are plotted in Fig. 21, which indicates how the lattice Pauli coefficients of Eq. (12) depend on the frequency detuning between control and target qubits Δ_{st}. Dashed black lines indicate static divergences that exist in the circuit in the static undriven circuit. In contrast, the dashed blue lines represent new divergences that appear in the microwave-activated part.

[1] J. Preskill, Quantum computing in the NISQ era and beyond, Quantum **2**, 79 (2018).

[2] K. Bharti, A. Cervera-Lierta, T. H. Kyaw, T. Haug, S. Alperin-Lea, A. Anand, M. Degroote, H. Heimonen, J. S. Kottmann, T. Menke, W.-K. Mok, S. Sim, L.-C. Kwek, and A. Aspuru-Guzik, Noisy intermediate-scale quantum algorithms, Rev. Mod. Phys. **94**, 015004 (2022).

[3] G. González-García, R. Trivedi, and J. I. Cirac, Error propagation in NISQ devices for solving classical optimization problems, PRX Quantum **3**, 040326 (2022).

[4] M. Malekakhlagh, E. Magesan, and D. C. McKay, First-principles analysis of cross-resonance gate operation, Phys. Rev. A **102**, 042605 (2020).

[5] N. Sundaresan, I. Lauer, E. Pritchett, E. Magesan, P. Jurcevic, and J. M. Gambetta, Reducing unitary and spectator errors in cross resonance with optimized rotary echoes, PRX Quantum **1**, 020318 (2020).

[6] T.-Q. Cai, X.-Y. Han, Y.-K. Wu, Y.-L. Ma, J.-H. Wang, Z.-L. Wang, H.-Y. Zhang, H.-Y. Wang, Y.-P. Song, and L.-M. Duan, Impact of spectators on a two-qubit gate in a tunable coupling superconducting circuit, Phys. Rev. Lett. **127**, 060505 (2021).

[7] J. B. Hertzberg, E. J. Zhang, S. Rosenblatt, E. Magesan, J. A. Smolin, J.-B. Yau, V. P. Adiga, M. Sandberg, M. Brink, J. M. Chow, and J. S. Orcutt, Laser-annealing Josephson junctions for yielding scaled-up superconducting quantum processors, Npj Quantum Inf. **7**, 129 (2021).

[8] V. Tripathi, H. Chen, M. Khezri, K.-W. Yip, E. Levenson-Falk, and D. A. Lidar, Suppression of crosstalk in superconducting qubits using dynamical decoupling, Phys. Rev. Appl. **18**, 024068 (2022).

[9] A. Morvan, L. Chen, J. M. Larson, D. I. Santiago, and I. Siddiqi, Optimizing frequency allocation for fixed-frequency superconducting quantum processors, Phys. Rev. Res. **4**, 023079 (2022).

[10] P. V. Klimov *et al.*, Optimizing quantum gates towards the scale of logical qubits, Nat. Commun. **15**, 2442 (2024).

[11] M. A. Nielsen and I. L. Chuang, *Quantum Computation and Quantum Information* (Cambridge University Press, Cambridge, 2000), 1st ed.

[12] I. M. Georgescu, S. Ashhab, and F. Nori, Quantum simulation, Rev. Mod. Phys. **86**, 153 (2014).

[13] J. Chu *et al.*, Scalable algorithm simplification using quantum and logic, Nat. Phys. **19**, 126 (2022).

[14] C. Fang, Y. Wang, K. Sun, and J. Kim, Realization of scalable Cirac-Zoller multi-qubit gates, arXiv:2301.07564.

[15] L. B. Nguyen, Y. Kim, A. Hashim, N. Goss, B. Marinelli, B. Bhandari, D. Das, R. K. Naik, J. M. Kreikebaum, A. N. Jordan, D. I. Santiago, and I. Siddiqi, Programmable Heisenberg interactions between Floquet qubits, Nat. Phys. **20**, 240 (2024).

[16] A. S. Nikolaeva, I. V. Zalivako, A. S. Borisenko, N. V. Semenin, K. P. Galstyan, A. E. Korolkov, E. O. Kiktenko, K. Y. Khabarova, I. A. Semerikov, A. K. Fedorov, and N. N. Kolachevsky, Scalable improvement of the generalized Toffoli gate realization using trapped-ion-based qutrits, arXiv:2407.07758.

[17] L. B. Nguyen, N. Goss, K. Siva, Y. Kim, E. Younis, B. Qing, A. Hashim, D. I. Santiago, and I. Siddiqi, Empowering a qudit-based quantum processor by traversing the dual bosonic ladder, Nat. Commun. **15**, 7117 (2024).

[18] Y. Kim, A. Morvan, L. B. Nguyen, R. K. Naik, C. Jünger, L. Chen, J. M. Kreikebaum, D. I. Santiago, and I. Siddiqi, High-fidelity three-qubit *i*Toffoli gate for fixed-frequency superconducting qubits, Nat. Phys. **18**, 783 (2022).

[19] A. J. Baker, G. B. P. Huber, N. J. Glaser, F. Roy, I. Tsitsilin, S. Filipp, and M. J. Hartmann, Single shot i-Toffoli gate in dispersively coupled superconducting qubits, Appl. Phys. Lett. **120**, 054002 (2022).

[20] N. J. Glaser, F. Roy, and S. Filipp, Controlled-controlled-phase gates for superconducting qubits mediated by a shared tunable coupler, Phys. Rev. Appl. **19**, 044001 (2023).

[21] R. Acharya *et al.*, Suppressing quantum errors by scaling a surface code logical qubit, Nature **614**, 676 (2023).

[22] Y. Cao, J. Romero, J. P. Olson, M. Degroote, P. D. Johnson, M. Kieferová, I. D. Kivlichan, T. Menke, B. Peropadre, N. P. D. Sawaya, S. Sim, L. Veis, and A. Aspuru-Guzik, Quantum chemistry in the age of quantum computing, Chem. Rev. **119**, 10856 (2019).

[23] J. Biamonte, P. Wittek, N. Pancotti, P. Rebentrost, N. Wiebe, and S. Lloyd, Quantum machine learning, Nature **549**, 195 (2017).

[24] J. Pazem and M. H. Ansari, Error mitigation of entangled states using brainbox quantum autoencoders, arXiv:2303.01134.

[25] A. Ciani, D. P. DiVincenzo, and B. M. Terhal, Lecture notes on quantum electrical circuits, arXiv:2312.05329.
[26] M. Reagor *et al.*, Demonstration of universal parametric entangling gates on a multi-qubit lattice, Sci. Adv. **4**, eaao3603 (2018).
[27] T. Menke, W. P. Banner, T. R. Bergamaschi, A. Di Paolo, A. Vepsäläinen, S. J. Weber, R. Winik, A. Melville, B. M. Niedzielski, D. Rosenberg, K. Serniak, M. E. Schwartz, J. L. Yoder, A. Aspuru-Guzik, S. Gustavsson, J. A. Grover, C. F. Hirjibehedin, A. J. Kerman, and W. D. Oliver, Demonstration of tunable three-body interactions between superconducting qubits, Phys. Rev. Lett. **129**, 220501 (2022).
[28] O. Katz, L. Feng, A. Risinger, C. Monroe, and M. Cetina, Demonstration of three- and four-body interactions between trapped-ion spins, Nat. Phys. **19**, 1452 (2023).
[29] M. Serbyn, Z. Papić, and D. A. Abanin, Local conservation laws and the structure of the many-body localized states, Phys. Rev. Lett. **111**, 127201 (2013).
[30] D. A. Huse, R. Nandkishore, and V. Oganesyan, Phenomenology of fully many-body-localized systems, Phys. Rev. B **90**, 174202 (2014).
[31] M. Schreiber, S. S. Hodgman, P. Bordia, H. P. Lüschen, M. H. Fischer, R. Vosk, E. Altman, U. Schneider, and I. Bloch, Observation of many-body localization of interacting fermions in a quasirandom optical lattice, Science **349**, 842 (2015).
[32] C. Berke, E. Varvelis, S. Trebst, A. Altland, and D. P. DiVincenzo, Transmon platform for quantum computing challenged by chaotic fluctuations, Nat. Commun. **13**, 2495 (2022).
[33] M. Lu, J. L. Ville, J. Cohen, A. Petrescu, S. Schreppler, L. Chen, C. Jünger, C. Pelletti, A. Marchenkov, A. Banerjee, W. Livingston, J. M. Kreikebaum, D. Santiago, A. Blais, and I. Siddiqi, Multipartite entanglement in Rabi driven superconducting qubits, arXiv:2207.00130.
[34] A. G. Fowler, M. Mariantoni, J. M. Martinis, and A. N. Cleland, Surface codes: Towards practical large-scale quantum computation, Phys. Rev. A **86**, 032324 (2012).
[35] T.-Y. Wu, A. Kumar, F. Giraldo, and D. S. Weiss, Stern–Gerlach detection of neutral-atom qubits in a state-dependent optical lattice, Nat. Phys. **15**, 538 (2019).
[36] A. Erhard, H. Poulsen Nautrup, M. Meth, L. Postler, R. Stricker, M. Stadler, V. Negnevitsky, M. Ringbauer, P. Schindler, H. J. Briegel, R. Blatt, N. Friis, and T. Monz, Entangling logical qubits with lattice surgery, Nature **589**, 220 (2021).
[37] C. Chamberland, A. Kubica, T. J. Yoder, and G. Zhu, Triangular color codes on trivalent graphs with flag qubits, New J. Phys. **22**, 023019 (2020).
[38] C. Chamberland and K. Noh, Very low overhead fault-tolerant magic state preparation using redundant ancilla encoding and flag qubits, Npj Quantum Inf. **6**, 91 (2020).
[39] K. Sahay and B. J. Brown, Decoder for the triangular color code by matching on a Möbius strip, PRX Quantum **3**, 010310 (2022).
[40] S. Rasmussen, K. Christensen, S. Pedersen, L. Kristensen, T. Bækkegaard, N. Loft, and N. Zinner, Superconducting circuit companion—An introduction with worked examples, PRX Quantum **2**, 040204 (2021).
[41] P. Krantz, M. Kjaergaard, F. Yan, T. P. Orlando, S. Gustavsson, and W. D. Oliver, A quantum engineer's guide to superconducting qubits, Appl. Phys. Rev. **6**, 021318 (2019).
[42] S. E. Nigg, H. Paik, B. Vlastakis, G. Kirchmair, S. Shankar, L. Frunzio, M. H. Devoret, R. J. Schoelkopf, and S. M. Girvin, Black-box superconducting circuit quantization, Phys. Rev. Lett. **108**, 240502 (2012).
[43] M. H. Ansari, Superconducting qubits beyond the dispersive regime, Phys. Rev. B **100**, 024509 (2019).
[44] J. Ku, X. Xu, M. Brink, D. C. McKay, J. B. Hertzberg, M. H. Ansari, and B. L. T. Plourde, Suppression of unwanted *ZZ* interactions in a hybrid two-qubit system, Phys. Rev. Lett. **125**, 200504 (2020).
[45] X. Xu and M. H. Ansari, *ZZ* freedom in two-qubit gates, Phys. Rev. Appl. **15**, 064074 (2021).
[46] T. Roy, S. Kundu, M. Chand, S. Hazra, N. Nehra, R. Cosmic, A. Ranadive, M. P. Patankar, K. Damle, and R. Vijay, Implementation of pairwise longitudinal coupling in a three-qubit superconducting circuit, Phys. Rev. Appl. **7**, 054025 (2017).
[47] E. Magesan and J. M. Gambetta, Effective Hamiltonian models of the cross-resonance gate, Phys. Rev. A **101**, 052308 (2020).
[48] L. S. Cederbaum, J. Schirmer, and H. D. Meyer, Block diagonalisation of Hermitian matrices, J. Phys. A: Math. Gen. **22**, 2427 (1989).
[49] Cirqubit (https://cirqubit.com), software suite for simulating superconducting qubits, (2024).
[50] G. S. Paraoanu, Microwave-induced coupling of superconducting qubits, Phys. Rev. B **74**, 140504(R) (2006).
[51] C. Rigetti and M. Devoret, Fully microwave-tunable universal gates in superconducting qubits with linear couplings and fixed transition frequencies, Phys. Rev. B **81**, 134507 (2010).
[52] Y. Xu, J. Chu, J. Yuan, J. Qiu, Y. Zhou, L. Zhang, X. Tan, Y. Yu, S. Liu, J. Li, F. Yan, and D. Yu, High-fidelity, high-scalability two-qubit gate scheme for superconducting qubits, Phys. Rev. Lett. **125**, 240503 (2020).
[53] A. Kandala, K. X. Wei, S. Srinivasan, E. Magesan, S. Carnevale, G. A. Keefe, D. Klaus, O. Dial, and D. C. McKay, Demonstration of a high-fidelity CNOT gate for fixed-frequency transmons with engineered *ZZ* suppression, Phys. Rev. Lett. **127**, 130501 (2021).
[54] X. Xu and M. Ansari, Parasitic-free gate: An error-protected cross-resonance switch in weakly tunable architectures, Phys. Rev. Appl. **19**, 024057 (2023).
[55] M. Ansari and X. Xu, Circuit with coupled qubits with different anharmonic energy spectrum, https://patents.google.com/patent/DE102020201688B3/en?inventor=xuexin+xu&oq=xuexin+xu German Patent DE102020201688B3 (issued Jul. 29, 2021).
[56] M. Ansari and X. Xu, Method of operating a circuit with a first and a second qubit, https://patents.google.com/patent/DE102020122245A1/en?inventor=Xuexin+Xu German Patent DE102020122245A1 (issued Mar. 3, 2022).